PLANT SCIENCE

Plant "helper" immune receptors are Ca²⁺-permeable nonselective cation channels

Pierre Jacob[1]†, Nak Hyun Kim[1]†, Feihua Wu[2,3], Farid El-Kasmi[4], Yuan Chi[2], William G. Walton[5], Oliver J. Furzer[1], Adam D. Lietzan[6], Sruthi Sunil[4], Korina Kempthorn[1], Matthew R. Redinbo[5], Zhen-Ming Pei[2]*, Li Wan[1,7]*, Jeffery L. Dangl[1]*

Plant nucleotide-binding leucine-rich repeat receptors (NLRs) regulate immunity and cell death. In *Arabidopsis*, a subfamily of "helper" NLRs is required by many "sensor" NLRs. Active NRG1.1 oligomerized, was enriched in plasma membrane puncta, and conferred cytoplasmic calcium ion (Ca²⁺) influx in plant and human cells. NRG1.1-dependent Ca²⁺ influx and cell death were sensitive to Ca²⁺ channel blockers and were suppressed by mutations affecting oligomerization or plasma membrane enrichment. Ca²⁺ influx and cell death mediated by NRG1.1 and ACTIVATED DISEASE RESISTANCE 1 (ADR1), another helper NLR, required conserved negatively charged N-terminal residues. Whole-cell voltage-clamp recordings demonstrated that *Arabidopsis* helper NLRs form Ca²⁺-permeable cation channels to directly regulate cytoplasmic Ca²⁺ levels and consequent cell death. Thus, helper NLRs transduce cell death signals directly.

In plants, successful pathogens inject effectors into the host cell to dampen the immune response. Plants evolved a surveillance system consisting of intracellular nucleotide–binding leucine-rich repeat receptors (NLRs) capable of triggering immunity in response to effector activity or by direct effector recognition (1). Effector-triggered immunity leads to activation of pathogen defense and culminates in the death of the host cell, the "hypersensitive response," which can further limit pathogen growth (2). NLR activation is sufficient to determine the outcome of a plant-pathogen interaction (1). In plants, NLRs are divided into two major classes based on their N-terminal domains: Toll/interleukin-1 receptor/Resistance (TIR)-NLRs, (hereafter, TNL) and the coiled-coil (CC)-NLRs (hereafter, CNL) (3, 4). All tested TNLs require ENHANCED DISEASE SUSCEPTIBILITY 1 (EDS1), as well as a subfamily of five redundant "helper" NLRs also known as RNLs because of their CC-R [RPW8 (Resistance to Powdery Mildew 8)-like CC] domain (5–7). There are two subfamilies of RNLs, NRG1 (N REQUIREMENT GENE 1) and ADR1 (ACTIVATED DISEASE RESISTANCE 1), in nearly all flowering plants (8).

Activation of the *Arabidopsis* RNL NRG1.1 can be mimicked using an autoactive allele (D485V; hereafter DV), mutated in the conserved methionine-histidine-aspartate motif. This is an accepted proxy for pathogen effector–mediated NLR activation (9–12). NRG1.1 DV–induced cell death is independent of the native RNLs NRG1 and ADR1 and of the EDS1-signaling module in the heterologous host, *Nicotiana benthamiana* [(4, 7, 13, 14); fig. S1].

Results

Structure of NRG1.1-signaling domain

We obtained x-ray crystal structures of two mutant NRG1.1 CC-R domains (residues 1 to 124), K94E/K96E/R99E/K100E/R103E/K106E/K110E [7K(R)/E] and K94E/K96E (2K/E), which diffracted to 3.0 and 2.5 Å, respectively (table S1). These putative surface mutations were required to achieve monodispersion of the protein. Structural homology modeling suggested that the CC-R domains share an N-terminal four-helical bundle with cell death pore forming mammalian mixed-linage kinase domain-like (MLKL) proteins and fungal HET-s/HELO domain proteins (6, 15, 16). Similar to predictions, the two mutant structures superimposed well with the four-helical bundles of the resting-state CC domain of ZAR1 (17) and the cation channel-forming domain of MLKL (18) (Fig. 1, A to D, and table S2).

The four-helical bundle of MLKL is sufficient to cause cell death, and this requires two hydrophobic residues, L58 and I76, which maintain the four-helical bundle hydrophobic core (19). Structural overlay predicted that the two hydrophobic residues are conserved in NRG1.1 as L69 and F86 (Fig. 1E); mutating them abolished cell death activity of an NRG1.1 fragment from residues 1 to 180 (hereafter NRG1.1 1-180) (Fig. 1F). In ZAR1, a hydrophobic groove
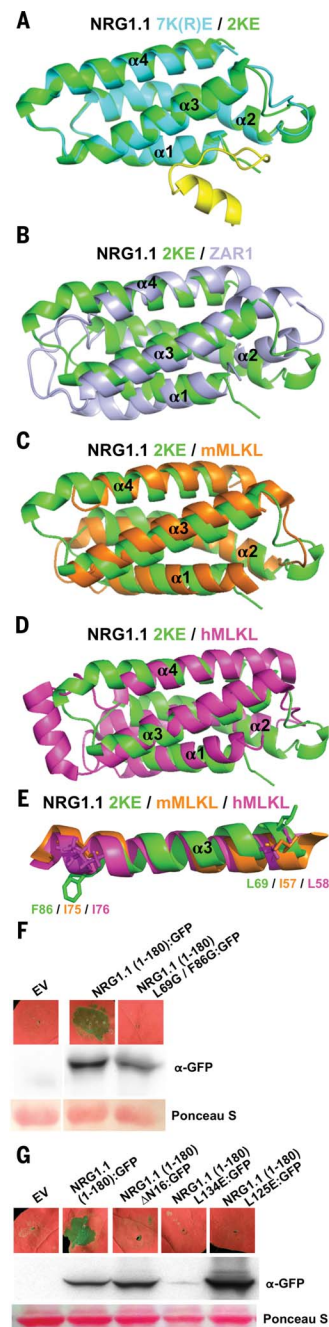
Fig. 1. NRG1.1 CC-R resembles the ZAR1 and MLKL four-helical bundle. (A) Structural overlay of 7K(R)E (PBD: 7L7V) and 2KE (7L7W) with 2KE in green, 7K(R)E four-helical bundle (4HB) in cyan, and 7K(R)E N-terminal region in yellow. (B) Structural overlay of 2KE in green and the ZAR1 4HB (6J5V) structure in light purple. (C) Structural overlay of 2KE in green and mMLKL 4HB (4BTF) in orange. (D) Structural overlay of 2KE in green and hMLKL 4HB (2MSV) in magenta. (E) Conserved F86/I75/I76 and L69/I57/L58 shown in sticks in the α3 helix of superimposed 2KE, mMLKL and hMLKL 4HB structures, respectively. (F and G) In planta (N. benthamiana) phenotypes at 2 days after induction and protein accumulation of WT NRG1.1 CC-R and structure-derived mutants. EV, empty vector.

made by α2 and α4B is important for oligomerization and function (*17*). We found two hydrophobic residues, L134 and L125, in the homologous region in NRG1.1; mutating them to glutamic acid abolished cell death in NRG1.1 1-180 (Fig. 1G). These data validate the NRG1.1 four-helical bundle structure.

Active ZAR1 oligomerizes into a pentamer in which the α1 helix of the four-helical bundle rearranges, flips out, and forms a plasma membrane (PM)–penetrating, funnel-like structure (*17, 20, 21*), consistent with models proposed for fungal Het-s/HELO activation (*22*). This first helix was essential for ZAR1 function at

the PM (*17*). One of the NRG1.1 CC-R structures [7(K)R/E] revealed a potentially flexible N terminus (residues 1 to 16; absent in ZAR1; Fig. 1A) that could extend the four-helical bundle α1 helix of a putative funnel in the active NRG1.1 protein. This was disordered in the 2K/E structure. This region was required for NRG1.1 1-180 cell death induction (ΔN16; Fig. 1G).

Active NRG1.1 oligomerizes and forms puncta

We introduced several of the structure-derived mutations into the full-length NRG1.1 in *cis* with the autoactive DV allele because the wild-type (WT) resting NRG1.1 is inactive in the absence

of sensor NLR activation (Fig. 2A). We found that the ΔN16, L134E, and L125E *cis* mutations each abolished the cell death function of NRG1.1 DV (Fig. 2A). Blue native-PAGE analyses revealed that active NRG1.1 DV formed high-molecular-weight complexes, whereas the inactive WT, catalytic p-loop (G199A/K200A), and DV p-loop *cis* double mutants did not (Fig. 2B). Mutation of L134E, but not of L125E, in *cis* also abolished NRG1.1 DV oligomer formation (Fig. 2B). Unlike the WT or inactive p-loop mutants, NRG1.1 DV was enriched in the PM fraction, whereas DV L125E showed substantially reduced PM enrichment (Fig. 2C). Although it

Fig. 2. Active NRG1.1 (D485V) oligomerizes on the PM and triggers cell death. (**A**) In planta phenotypes of NRG1.1 variants in *N. benthamiana* (*Nb*) at 2 dpi. YFP, yellow fluorescent protein. (**B**) Oligomerization of NRG1.1 DV variants. Accumulation of YFP-tagged NRG1.1 variants was verified by SDS–polyacrylamide gel electrophoresis (PAGE) immunoblotting, and their oligomeric states were checked by blue native-PAGE immunoblotting in *Nb adr1 nrg1*. (**C**) Activation promotes PM enrichment. Total proteins (T) extracted from *Nb*-expressing NRG1.1:YFP variants were fractionated into cytosolic (C), total membrane (TM), and PM fractions and verified by marker proteins: Cytosol, cytosolic ascorbic peroxidase; endoplasmic reticulum membrane (EM), sterol methyltransferase 1; PM, H+ATPase.
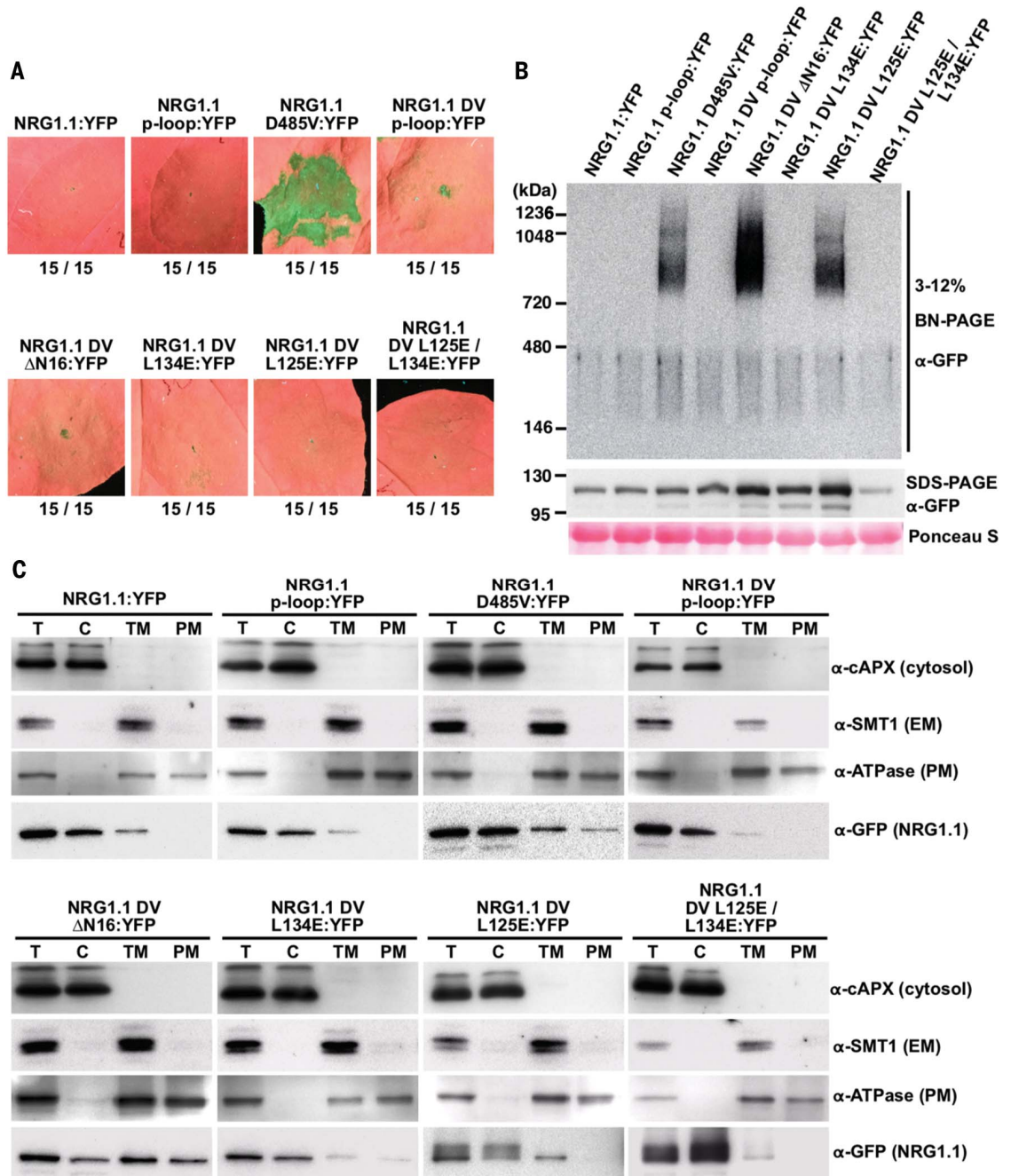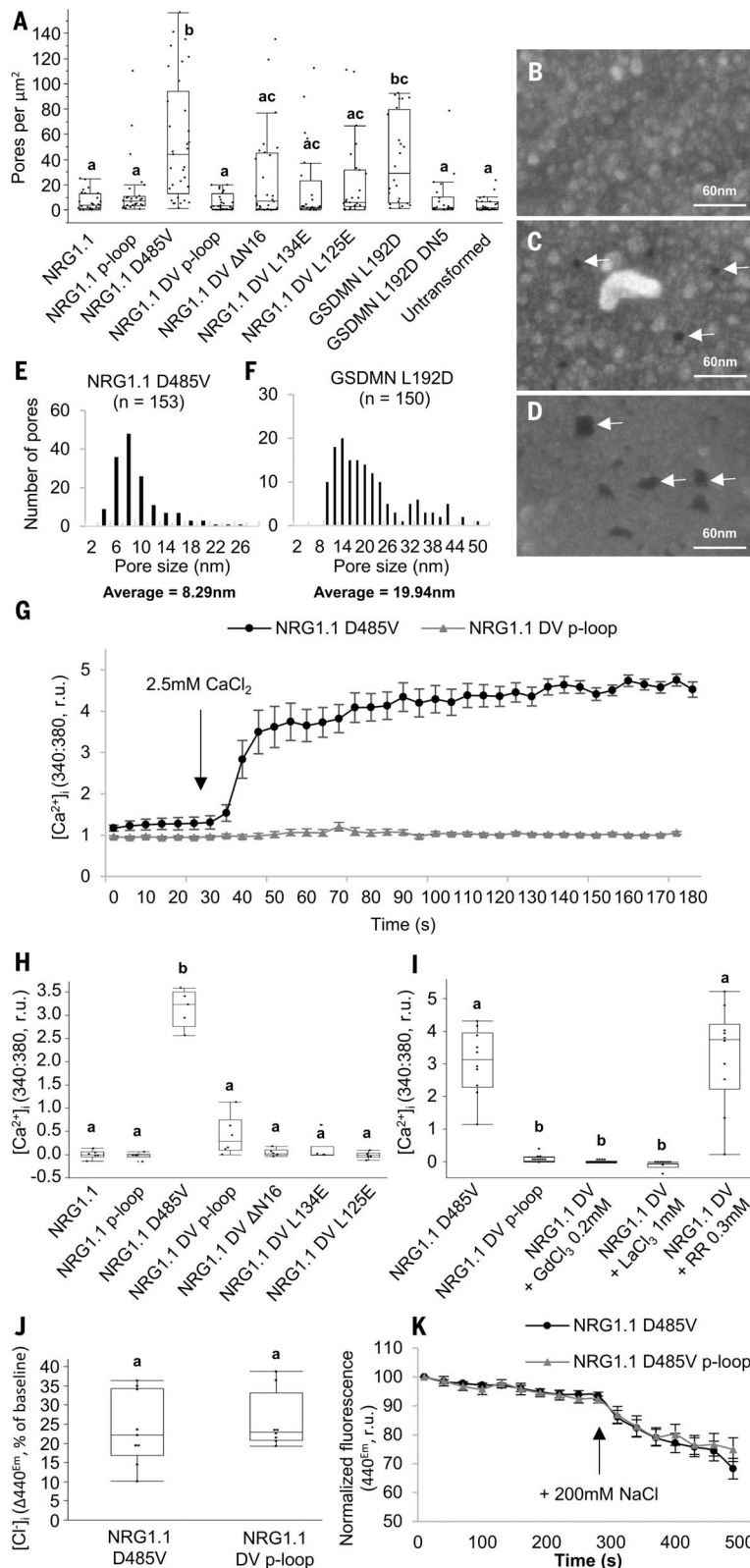
Fig. 3. NRG1.1 forms ion channels permeable to Ca²⁺ and not Cl⁻. (**A**) Quantification of apparent PM pores in HeLa cells expressing NRG1.1 variants. (**B** to **D**) Representative scanning electron micrographs of cells exhibiting apparent PM pores in cell lines expressing the NRG1.1 DV p-loop (B), NRG1.1 D485V (C) or the pore-forming protein GSDMN 1-275 L192D (D). White arrows indicate the visible PM pores. (**E** and **F**) Distribution of the diameter of PM pores visible after NRG1.1 D485V (E) or GSDMN L192D (F) expression. The average diameters are significantly different (t test, $P < 0.0001$). (**G**) [Ca^{2+}]$_i$ in NRG1.1 D485V or NRG1.1 D485V p-loop–expressing HeLa cells. Black arrow indicates $CaCl_2$ addition. (**H**) Ca^{2+} influx in HeLa cells expressing NRG1.1 variants. (**I**) Effect of the Ca^{2+} channel blockers $LaCl_3$, $GdCl_3$, and ruthenium red (RR) on NRG1.1 D485V–induced Ca^{2+} influx. (**J**) Intracellular [Cl^-] accumulation in cells expressing the NRG1.1 D485V or NRG1.1 DV p-loop. (**K**) Representative time course experiment showing variation of [Cl^-]. Black arrow indicates 200 mM NaCl addition. Letters indicate statistical significance (ANOVA with post hoc Tukey, $P < 0.01$).

the NRG1.1 DV ΔN16 double mutant but were less common for the missense loss-of-function alleles, which colocalized more with the endoplasmic reticulum marker than the PM marker (fig. S3). These results show that the NRG1.1 N-terminal 16 residues may extend a funnel-like structure similar to that of ZAR1.
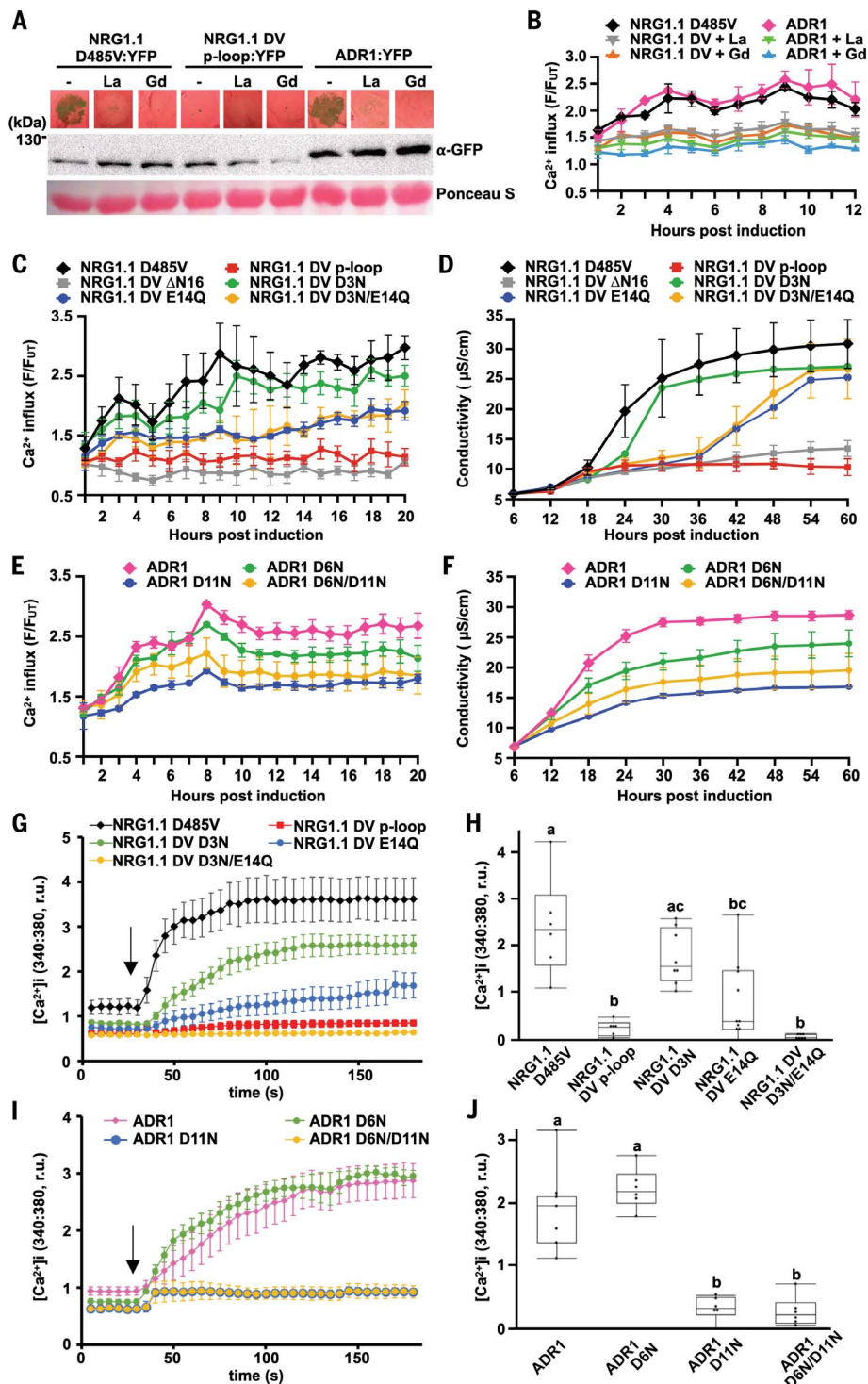
NRG1.1 is functional in human HeLa cells

We investigated the possibility that NRG1.1 forms PM pores and functions as a channel. We expressed NRG1.1 variants in HeLa cells. If NRG1.1 caused cell death, formed pores, and exhibited channel activity in this evolutionarily distant cellular background, then the most parsimonious conclusion would be that it did so autonomously. The alternative hypothesis would require a signaling partner conserved between plants and humans. NRG1.1 DV induced significant cell death at 6 hours after induction (fig. S5). This did not occur when WT NRG1.1 was expressed or when NRG1.1 DV activity was suppressed by p-loop, ΔN16, L125E, or L134E mutations in *cis* (fig. S5). Oligomerization and PM localization of the NRG1.1 variants in HeLa cells were similar to the in planta results (fig. S6). Thus, the genetic requirements for NRG1.1 DV cell death initiation, (p-loop, N16, L125, and L134) are similar in HeLa cells and plant cells.

We observed the morphology of the dying HeLa cells using scanning electron microscopy. We found that the number of PM pores, appearing as dark spots (*23*), correlated with the cell death activity of NRG1.1 variants (fig. S7 and Fig. 3, A to C). NRG1.1 DV–expressing cells exhibited 8-nm (average) pores in these processed samples (Fig. 3, E and F), although

oligomerized and was enriched at the PM (figs. S2 to S4), NRG1.1 DV ΔN16 failed to induce cell death (Fig. 2, A to C).

Confocal microscopy demonstrated that NRG1.1 DV exhibits increased PM localization compared with inactive alleles (figs. S2 to S4). Active NRG1.1 DV exhibited numerous puncta on the PM, whereas the NRG1.1 DV p-loop double mutant exhibited many fewer (figs. S2 to S4). These puncta were also observed for

Fig. 4. Negatively charged residues in the conserved RNL motif are required for Ca^{2+} influx and cell death. (**A**) In planta phenotypes (2 dpi) of plant RNLs in the presence of the Ca^{2+} channel blockers $LaCl_3$ (La) and $GdCl_3$ (Gd). Accumulation of YFP-tagged RNL variants was verified by SDS-PAGE and-immunoblotting, in *Nb adr1 nrg1*. (**B**, **C**, and **E**) Time course RNL-induced Ca^{2+} influx measurements with GCaMP3-transgenic *Nb*. (**D** and **F**) Time course conductivity measurement depicting RNL-triggered cell death in *Nb*. (**G** to **J**) $[Ca^{2+}]_i$ in HeLa cells expressing NRG1.1 DV and variants (G and H) or ADR1 and variants (I and J). Black arrows indicate the addition of $CaCl_2$. Letters indicate statistical significance (ANOVA with post hoc Tukey, $P < 0.05$). YFP-tagged RNL protein expression in *Nb* and HeLa cells was verified (fig. S16).

(*25*, *26*) and is a requirement for NLR signaling (*25*, *27*). Using Fura-2–based Ca^{2+} imaging (*28*, *29*), we measured the cytosolic free Ca^{2+} concentration ($[Ca^{2+}]_i$) in HeLa cells expressing NRG1.1 DV or the DV p-loop double mutant to determine whether NRG1.1 DV affected cytoplasmic Ca^{2+} homeostasis. We observed sustained $[Ca^{2+}]_i$ increases specifically in the NRG1.1 DV–expressing cells seconds after $CaCl_2$ addition (Fig. 3G and fig. S8). Loss of the cell death *cis* mutations ΔN16, L125E, or L134E all suppressed NRG1.1 DV–driven Ca^{2+} influx (Fig. 3H and fig. S8). The general Ca^{2+} influx channel blockers $LaCl_3$ and $GdCl_3$, but not the Ca^{2+} release channel blocker ruthenium red (*30*–*32*), blocked NRG1.1 DV–driven Ca^{2+} influx (Fig. 3I and fig. S9). These observations are consistent with NRG1.1 DV directly or indirectly facilitating Ca^{2+} influx. We investigated the specificity of NRG1.1 DV–driven ion flux by measuring cytosolic $[Cl^-]$ using 6-methoxy-N-ethylquinolinium iodide (MEQ)/dihydroMEQ (*33*). There was no difference between the NRG1.1 DV and NRG1.1 DV p-loop–expressing cells (Fig. 3, J and K, and fig. S10), indicating that NRG1.1 DV channels do not drive Cl^- influx. Thus, we conclude that NRG1.1 might form Ca^{2+}-permeable channels, or facilitate their formation, in the PM of HeLa cells.

Conserved negatively charged RNL residues are required for Ca^{2+} influx

We focused on the first 16 amino acids of NRG1.1 across 334 plant RNL sequences because NRG1.1 DV ΔN16 retained oligomerization and PM enrichment but lost Ca^{2+} influx. We observed a pattern of glycine or negatively charged or polar residues separated by two to three hydrophobic residues (table S3 and fig. S11). This motif was conserved in the ADR1 clade of RNLs, partially degenerated in the NRG1 clade, and further degenerated in CNLs (fig. S12). Although different from an

this may not represent the actual pore size. This apparent pore size was significantly different from the size of larger pores formed by GASDERMIN-D 1-275 L192D, a partial loss-of-function mutant of the pore-forming protein GASDERMIN-D that induces cell death and allows high protein accumulation [(*17*, *24*); Fig. 3, D to F, and fig. S5B]. Cell fractionation experiments indicated that NRG1.1 DV was

enriched in the PM fraction in HeLa cells, whereas the NRG1.1 DV p-loop *cis* double mutant was not (fig. S6B). Overall, active NRG1.1 DV localized to the PM and its cell death activity was associated with the occurrence of PM pores in HeLa cells.

Helper NLRs form Ca^{2+}-permeable channels

Ca^{2+} influx is a hallmark of programmed cell death in both the animal and plant kingdoms

N-terminal motif recently implicated in CNL function (*34*), these two domains share regularly spaced, negatively charged residues. Such residues are critical for ion selectivity and permeability in Ca^{2+} channels (*35*, *36*). We targeted the negatively charged residues within the first 16 amino acids of NRG1.1 DV and the autoactive WT ADR1 (*37*) for structurally conservative but uncharged *cis* mutations (NRG1.1 DV: D3N, E14Q, or D3N/E14Q; ADR1: D6N, D11N, or D6N/D11N).

We assayed Ca^{2+} influx triggered by these alleles in planta using the intracellular Ca^{2+} reporter GCaMP3 in transgenic *N. benthamiana* (*38*). We confirmed that either NRG1.1 DV or ADR1 expression triggered $[Ca^{2+}]_i$ increases in planta 2 to 3 hours after estradiol treatment (a typical time required for estradiol-induced protein accumulation), which was accompanied by cell death 16 hours after $[Ca^{2+}]_i$ increase (Fig. 4, A and B). $LaCl_3$ and $GdCl_3$

abolished cell death (Fig. 4A) and reduced Ca^{2+} influx (Fig. 4B). In both plant (Fig. 4, C to F) and HeLa cells (Fig. 4, G to J), mutations in the RNL-conserved N-terminal motif, especially E14Q (in NRG1.1 DV) and D11N (in ADR1), significantly reduced the rate of Ca^{2+} influx (Fig. 4, C, E, and G to J, and fig. S13). These mutations also reduced cell death induction (Fig. 4, D and F, and figs. S14 and S15).

We analyzed the electrophysiological properties of NRG1.1 DV and NRG1.1 DV D3N E14Q in human embryonic kidney (HEK) 293 cells using the patch-clamp technique (*28*, *29*). Having confirmed that NRG1.1 DV drives Ca^{2+} influx in transfected HEK293 cells similar to HeLa cells using Fura-2 imaging (fig. S17), we proceeded to record whole-cell voltage-clamp currents with voltage ramp (from +50 mV to −200 mV). We recorded robust currents at both positive and negative potentials only in cells expressing NRG1.1 DV with CsCl and

$CaCl_2$ in the pipette and bath solution, respectively (Fig. 5, A and C). Both inward and outward currents were abolished when Cs^+ and Ca^{2+} were substituted for the channel-impermeable cation TEA^+ (Fig. 5, B and C), indicating that NRG1.1 DV formed nonselective cation channels mediating Ca^{2+} influx rather than Cl^- efflux. The NRG1.1 D3N E14Q double mutant eliminated Ca^{2+} currents (Fig. 5, A to C), consistent with D3 and/or E14 acting as a selectivity filter. Substitution of Mg^{2+} for Ca^{2+} in the bath resulted in a similar permeability for Mg^{2+} and Ca^{2+} (Fig. 5D), confirming that NRG1.1 is a nonselective, cation-permeable channel.

Discussion

Ca^{2+} signaling is known to regulate plant immunity (*26*, *39*). Constitutive cytoplasmic Ca^{2+} influx induces constitutive defense activation and cell death (*40*, *41*). We found that the NRG1.1-signaling domain structure resembles the pore-forming domain of the cation channel MLKL (Fig. 1), oligomerizes in puncta on the PM (Fig. 2), and is sufficient to drive cytoplasmic Ca^{2+} influx in plants and human cells (Figs. 3 to 5 and fig. S2). Our data are consistent with NRG1.1 acting as a nonselective, Ca^{2+}-permeable cation channel.

All TNL immune receptors tested so far required the redundant RNLs of the ADR1 and NRG1 subfamilies (*5*). Thus, we propose that TNL activation induces RNL-dependent Ca^{2+} influx to initiate cell death and, likely, immune responses. Supporting this view, we observed that TNL RPS4 activation is associated with Ca^{2+} influx (fig. S18). Cyclic nucleotide–gated channels may also contribute to sustain the RNL-initiated Ca^{2+} influx because they have been shown to be activated upon immune response (*42*). It is plausible that cell death is a product of Ca^{2+}-responsive factors that execute a cell death program rather than being a consequence of Ca^{2+} cytotoxicity. Cell death and defense activation can be uncoupled during effector-triggered immunity, suggesting that cell death has additional signaling requirements beyond elevated $[Ca^{2+}]$ (*2*, *43*). Plants have MLKL homologs that are involved in immunity and can trigger cell death (*44*), possibly by regulating ion homeostasis [Mg^{2+} rather than Ca^{2+} (*18*, *45*), by analogy with human MLKL].

CNLs likely also function like RNLs and trigger cytoplasmic Ca^{2+} influx. Recently, the CNL ZAR1 was shown to be a Ca^{2+}-permeable channel that requires a negative charge ring for cation influx (*21*). It is thus likely that ZAR1 E11, NRG1.1 E14, and ADR1 D11 all form negative charge rings that act as cation selective filters to achieve fast Ca^{2+} influx and initiation of cell death and defense signaling. The combined data from our work and (*21*) provide a mechanistic explanation for how the two major
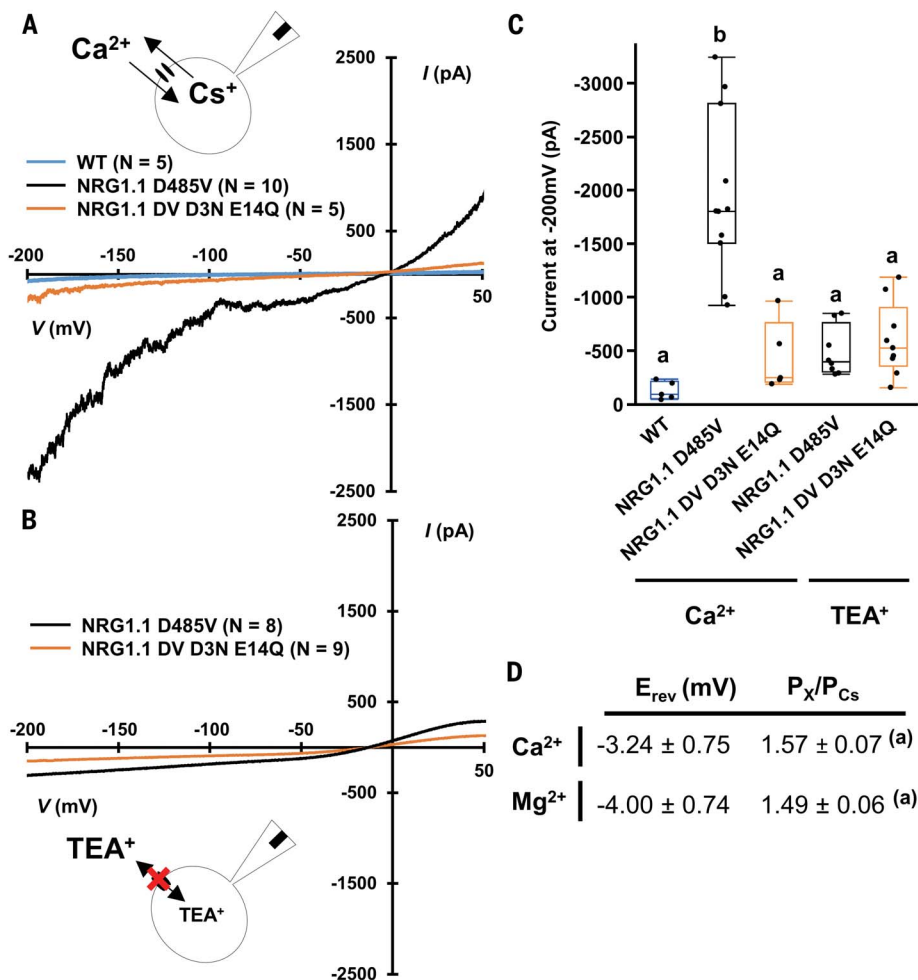

Fig. 5. NRG1.1 D485V forms nonselective cation channel. (**A**) Whole-cell current recorded in voltage ramp (+50 to −200 mV) in a $CaCl_2$ bath solution. (**B**) Whole-cell current recorded in voltage ramp (+50 to −200 mV) in a TEA-Cl bath solution. (**C**) Mean current recorded at −200 mV during experiments in (A) and (B). (**D**) Reversal potential (E_{rev}) and relative ion permeability (P_X/P_{Cs}) measured in voltage ramp experiments in $CaCl_2$ or $MgCl_2$ solutions in HEK293 cells expressing NRG1.1 D485V ($N = 10$ Ca^{2+} and $N = 8$ Mg^{2+}). Letters indicate statistical difference (ANOVA with post hoc Tukey, $P < 0.05$).

D

	E_{rev} (mV)	P_X/P_{Cs}
Ca^{2+}	−3.24 ± 0.75	1.57 ± 0.07 [a]
Mg^{2+}	−4.00 ± 0.74	1.49 ± 0.06 [a]

classes of plant intracellular innate immune receptors, the TNLs and CNLs, control cell death triggered by pathogen recognition.

REFERENCES AND NOTES

1. J. D. Jones, R. E. Vance, J. L. Dangl, *Science* **354**, aaf6395 (2016).
2. B. Laflamme *et al.*, *Science* **367**, 763–768 (2020).
3. J. Tamborski, K. V. Krasileva, *Annu. Rev. Plant Biol.* **71**, 355–378 (2020).
4. I. M. L. Saur, R. Panstruga, P. Schulze-Lefert, *Nat. Rev. Immunol.* **21**, 305–318 (2020).
5. S. C. Saile *et al.*, *PLOS Biol.* **18**, e3000783 (2020).
6. L. M. Jubic, S. Saile, O. J. Furzer, F. El Kasmi, J. L. Dangl, *Curr. Opin. Plant Biol.* **50**, 82–94 (2019).
7. D. Lapin, D. D. Bhandari, J. E. Parker, *Annu. Rev. Phytopathol.* **58**, 253–276 (2020).
8. C. Van Ghelder *et al.*, *Sci. Rep.* **9**, 11614 (2019).
9. D. T. N. Tran *et al.*, *Curr. Biol.* **27**, 1148–1160 (2017).
10. Z. Wu *et al.*, *New Phytol.* **222**, 938–953 (2019).
11. S. J. Williams *et al.*, *Mol. Plant Microbe Interact.* **24**, 897–906 (2011).
12. W. I. L. Tameling *et al.*, *Plant Physiol.* **140**, 1233–1245 (2006).
13. T. Qi *et al.*, *Proc. Natl. Acad. Sci. U.S.A.* **115**, E10979–E10987 (2018).
14. D. Lapin *et al.*, *Plant Cell* **31**, 2430–2455 (2019).
15. A. R. Bentham, R. Zdrzalek, J. C. De la Concepcion, M. J. Banfield, *Plant Cell Physiol.* **59**, 2398–2408 (2018).
16. A. Daskalov *et al.*, *Proc. Natl. Acad. Sci. U.S.A.* **113**, 2720–2725 (2016).
17. J. Wang *et al.*, *Science* **364**, eaav5870 (2019).
18. B. Xia *et al.*, *Cell Res.* **26**, 517–528 (2016).
19. Z. Cai *et al.*, *Nat. Cell Biol.* **16**, 55–65 (2014).
20. J. Wang *et al.*, *Science* **364**, eaav5868 (2019).
21. G. Bi *et al.*, *Cell* **184**, 3528–3541.e12 (2021).
22. C. Seuring *et al.*, *PLOS Biol.* **10**, e1001451 (2012).
23. D. R. Herr *et al.*, *Neuromolecular Med.* **22**, 293–303 (2020).
24. J. Ding *et al.*, *Nature* **535**, 111–116 (2016).
25. M. Huysmans, S. Lema A, N. S. Coll, M. K. Nowack, *Curr. Opin. Plant Biol.* **35**, 37–44 (2017).
26. W. Moeder, V. Phan, K. Yoshioka, *Plant Sci.* **279**, 19–26 (2019).
27. M. Grant *et al.*, *Plant J.* **23**, 441–450 (2000).
28. M. J. Caterina *et al.*, *Nature* **389**, 816–824 (1997).
29. F. Yuan *et al.*, *Nature* **514**, 367–371 (2014).
30. X. Gao *et al.*, *PLOS Pathog.* **9**, e1003127 (2013).
31. J. Castro, E. C. Aromataris, G. Y. Rychkov, G. J. Barritt, *Biochem. J.* **418**, 553–566 (2009).
32. K. De Vriese, A. Costa, T. Beeckman, S. Vanneste, *Int. J. Mol. Sci.* **19**, 1506 (2018).
33. J. R. Inglefield, R. D. Schwartz-Bloom, *Methods Enzymol.* **307**, 469–481 (1999).
34. H. Adachi *et al.*, *eLife* **8**, e49956 (2019).
35. L. Tang *et al.*, *Nature* **505**, 56–61 (2014).
36. M. Fan *et al.*, *Nature* **582**, 129–133 (2020).
37. O. X. Dong *et al.*, *New Phytol.* **210**, 960–973 (2016).
38. T. A. DeFalco *et al.*, *Plant Cell Physiol.* **58**, 1173–1184 (2017).
39. S. Stael *et al.*, *Trends Plant Sci.* **20**, 3–11 (2015).
40. K. Yoshioka *et al.*, *Plant Cell* **18**, 747–763 (2006).
41. C. Zhao *et al.*, *New Phytol.* **230**, 1078–1094 (2021).
42. W. Tian *et al.*, *Nature* **572**, 131–135 (2019).
43. W. Gassmann, *Mol. Plant Microbe Interact.* **18**, 1054–1060 (2005).
44. L. K. Mahdi *et al.*, *Cell Host Microbe* **28**, 813–824.e6 (2020).
45. U. Ros *et al.*, *Cell Rep.* **19**, 175–187 (2017).

Science

Plant "helper" immune receptors are Ca^{2+}-permeable nonselective cation channels

Pierre Jacob, Nak Hyun Kim, Feihua Wu, Farid El-Kasmi, Yuan Chi, William G. Walton, Oliver J. Furzer, Adam D. Lietzan, Sruthi Sunil, Korina Kempthorn, Matthew R. Redinbo, Zhen-Ming Pei, Li Wan and Jeffery L. Dangl

Calcium signaling for host cell death

In response to microbial pathogens, some plants kill off their own cells to limit further spread of infection. The Toll/Interleukin-1 receptor/Resistance class of nucleotide-binding leucine-rich repeat receptors (known as TNLs) function in plants as immune receptors. These TNLs work together with a dedicated set of helper proteins. Jacob *et al.* reveal the structure of one of these helpers known as NRG1 (N REQUIREMENT GENE 1). The structure resembles a known animal cation channel. The authors demonstrate that helper NLRs directly control calcium ion influx to initiate host cell death, providing a mechanism for TNL outputs.

Science, abg7917, this issue p. 420

ARTICLE TOOLS	http://science.sciencemag.org/content/373/6553/420
SUPPLEMENTARY MATERIALS	http://science.sciencemag.org/content/suppl/2021/06/16/science.abg7917.DC1
REFERENCES	This article cites 66 articles, 12 of which you can access for free http://science.sciencemag.org/content/373/6553/420#BIBL
PERMISSIONS	http://www.sciencemag.org/help/reprints-and-permissions

Use of this article is subject to the Terms of Service

Supplementary Materials for

Plant "helper" immune receptors are Ca^{2+}-permeable nonselective cation channels

Pierre Jacob†, Nak Hyun Kim†, Feihua Wu, Farid El-Kasmi, Yuan Chi, William G. Walton, Oliver J. Furzer, Adam D. Lietzan, Sruthi Sunil, Korina Kempthorn, Matthew R. Redinbo, Zhen-Ming Pei*, Li Wan*, Jeffery L. Dangl*

†These authors contributed equally to this work and are listed alphabetically.
*Corresponding author. Email: zpei@duke.edu (Z.-M.P.); lwan@cemps.ac.cn (L.W.); dangl@email.unc.edu (J.D.)

This PDF file includes:

Materials and Methods
Tables S1, S2, and S4
Figs. S1 to S18
References

Other Supplementary Material for this manuscript includes the following:
(available at science.sciencemag.org/cgi/content/full/science.abg7917/DC1)

Table S3 (Excel file)
MDAR Reproducibility Checklist (PDF)

Materials and Methods

Recombinant protein cloning, expression, and purification:

cDNA of *At*NRG1.1 CC 1-124 (WT, 2K/E and 7K(R)/E) was codon optimized for recombinant

5 protein expression in *E. coli* and subcloned into the pET24a plasmid (Genescript) with a N-terminal (His)$_6$ tag and C-terminal Strep II tag (WSHPQFEK). All proteins were produced in *E. coli* BL21 (DE3) cells using the autoinduction method (*46*) and purified to homogeneity using nickle affinity chromatography followed by size-exclusion chromatography. The selenomethionine (SeMet) incorporated form of 7K(R)/E was produced using SelenoMet^{TM}

10 medium from Molecular Dimensions and 0.1 mM isopropyl-1-thio-D-galactopyranoside (IPTG) for protein induction. Briefly, *E. coli* cells were grown at 37°C until the OD$_{600}$ reached 0.6. The temperature was then decreased to 18°C with protein induction for 18 hours. Cells were pelleted by centrifugation at 6000 x *g* at 4°C for 30 minutes. All cell pellets were resuspended in 5 mL of the lysis buffer (50 mM HEPES pH 8.0, 300 mM NaCl and 2 mM DTT) per gram of cell paste.

15 Phenylmethanesulfonylfluoride (PMSF; 1 mM final concentration), lysozyme, and DNase were added to the cell resuspension immediately prior to lysing. The resuspended cells were lysed using sonication and then centrifuged at 41, 211 x *g* for 20 minutes to remove cell debris. The supernatant was loaded onto a nickel HisTrap 5 mL column (GE Healthcare) pre-equilibrated with 20 mL of the wash buffer (50 mM HEPES pH 8.0, 300 mM NaCl, 30 mM imidazole) at a

20 rate of 3 mL/min. The column was then washed with 100 mL of wash buffer and the bound protein was eluted with elution buffer (50 mM HEPES pH 7.5, 300 mM NaCl, 500 mM imidazole). Elution fractions were monitored via A$_{280}$, elution peak pooled, and further purified using a S200 HiLoad 16/600 column pre-equilibrated with the gel-filtration buffer (10 mM HEPES pH 7.5, 150 mM NaCl and 1mM DTT). The A$_{280}$ elution peak fractions were confirmed

25 by SDS-PAGE, pooled, and the proteins were concentrated to a final concentration of 10 mg/mL. The concentrated proteins were flash-frozen as 30 μL aliquots in liquid nitrogen and stored at -80°C.

Protein crystallization, data collection, and structure determination:

All proteins were crystallized using the sitting drop vapor diffusion technique. A protein solution consisting of ~10 mg/mL 7K(R)/E native or 7K(R)/E SeMet was mixed at a 1:1 ratio with a precipitant solution composed of 0.1 M MES (pH 5.5) and 1 M potassium sodium tartrate. 7K(R)/E crystals formed within 3 days. Similarly, crystals of 2K/E were produced by mixing a 1:1 ratio of ~10 mg/mL protein solution with a precipitant solution consisting of 0.1 M HEPES: NaOH (pH 7.5) and 0.3 M magnesium formate. 2K/E crystals formed within 2 days.

Protein crystals of 7K(R)/E native were transferred directly into a mother liquor consisting of the well solution supplemented with ethylene glycol to a final concentration of 20% (v/v). Likewise, 7K(R)/E SeMet and 2K/E crystals were transferred into a mother liquor consisting of the well solution supplemented with glycerol to a final concentration of 20% (v/v). Once transferred, crystals were immediately flash cooled in liquid nitrogen in preparation for x-ray diffraction data collection.

X-ray diffraction data for the 7K(R)/E SeMet construct (M1, M45, M58, and M98) were collected from a single crystal at the 23-IDD beamline using a wavelength tuned to 0.979 Å. Diffraction images were processed with the HKL2000 suite (*47*) and the structure was solved using the single-wavelength anomalous diffraction (SAD) method through the *Autosol* pipeline within the *PHENIX* suite. An initial model was built using the *Autobuild* pipeline within the *PHENIX* suite (*48*). X-ray diffraction data for native crystals of 7K(R)/E were collected at the 23-IDD beamline to a higher resolution than that of the 7K(R)/E SeMet crystals. The native 7K(R)/E diffraction images were processed using the HKL2000 suite and the structure was subsequently solved by molecular replacement using PHASER (*49*) with the 7K(R)/E SeMet build as a search model. X-ray diffraction data for 2K/E were collected at the 23-IDD beamline and the structure was solved by molecular replacement using PHASER with 7K(R)/E as the search model. All models were extended by several rounds of manual model building with COOT (*50*). Successive refinements were performed with Phenix.refine or REFMAC within the

CCP4 suite (*48, 51*). Structural analyses were carried out using DALI (*52*) and PyMOL (http://www.pymol.org). Figures were generated using PyMOL. Structures of 7K(R)/E native and 2K/E native are available in the PDB as accessions 7L7V and 7L7W，respectively.

DNA constructs and vectors used:

5   The *NRG1.1* CDS (wildtype and all analyzed mutants) were synthesized into a pUC57/Kan plasmid (Genescript) including the gateway compatible recombination sites (attR1/attR2). LR reactions (Gateway Cloning Technology, Life Technologies; Carlsbad, USA) were performed to introduce CDS's into the estradiol-inducible destination vector pMDC7 with a C-terminal YFP-HA CDS (*53*), or the 35s-driven destination vector pGWB641 (*54*). The clones of NRG1.1 1-

10   180, ΔN16 and structure-derived mutants (all C-terminal GFP-fusions) were constructed in pICSL86922 (35S promoter and TMV omega enhancer) using Golden Gate cloning (*55*).

Bacterial strains and growth conditions.

Agrobacterium tumefaciens strain GV3101/pMP90 were grown in LB media at 28°**C**. Antibiotic concentrations used (in g/mL) Kanamycin 100, Gentamycin 50 and Spectinomycin 100,

15   Rifampicin 100. Constructs were transformed into *Agrobacterium tumefaciens* strain GV3101/pMP90 and used for transient expression in *Nicotiana benthamiana*. NRG1.1 WT and variants were transiently expressed in *Nicotiana benthamiana*.

Determination of NRG1.1 localization using confocal imaging:

Briefly, *Agrobacterium tumefaciens* strains were grown overnight at 28°C in LB media

20   containing the appropriate antibiotics. The overnight cultures were centrifuged for 8 min at 8,500 rpm and the pellets were resuspended in induction buffer (10 mM $MgCl_2$, 10 mM MES pH 5.6, 150 μM acetosyringone). The OD_{600} was adjusted to 0.05 (35S::P19) and 0.3 for NRG1.1 constructs and the specific subcellular marker constructs (35S::BRI1-mRFP – a gift from Klaus Harter, UBQ10::VMA12-RFP – a gift from Karen Schuhmacher – and 35S::PLC2-CFP).

25   Samples were mixed as indicated. Agrobacteria mixtures were infiltrated into young leaves of 4-6 weeks old *N. benthamiana* WT plants using a 1-ml needleless syringe. The *N. benthamiana* plants were grown on soil under 12h light / 12h dark cycles (24°C/22°C, 65% humidity). Induction was done 24 hours post infiltration using either 20 μM β-estradiol (Sigma-Aldrich; St.

4

Louis, USA) and 0.001% [v/v] Silwet L-77 by spraying. Leaves were imaged for protein localization between 6 h- 24 h post induction with the confocal laser scanning microscope LSM880 from Zeiss (Oberkochen, Germany), using C-apochromat 40x or 63x/1.2 W Korr FCS M27 water-immersion objectives and the ZENblack software. YFP was excited using a 514 nm laser collecting emission between 516-556 nm; RFP was excited using a 561 nm laser with an emission spectrum of 597-633 nm, CFP was excited with a 458 nm laser and the emission spectrum was 463-513 nm. Focal plane images were processed with the ZENblue software (Zeiss) for adjustment of brightness and contrast. Maximum Z-projection images were processed with ImageJ/Fiji (56).

UV-light imaging of cell death phenotypes:

Briefly, *A. tumefaciens* strains were infiltrated into *N. benthamiana* leaves as described above. The OD_{600} was adjusted to 0.1 (35S::P19) and 0.8 for NRG1.1 and ADR1 constructs. For Ca^{2+} inhibitor treatments, 2 mM $LaCl_3$ or $GdCl_3$ was added to the infiltration media prior to infiltration. Induction was done 24 hours post infiltration using 100 μM β-estradiol (Sigma-Aldrich; St. Louis, USA) and 0.002% [v/v] Silwet L-77 by spraying. 1-2 days post induction the leaves were placed under UV lamps (B-100AP, UVP) and photographed using a digital camera with a yellow filter.

In planta semi-quantification of Ca^{2+} influx:

Briefly, *A. tumefaciens* strains were infiltrated into transgenic GCaMP3 *N. benthamiana* (38) leaves and protein expression induced as described above. Leaf discs (0.5 cm diameter) were placed on 200 uL ddH_2O in Nunclon 96 Flat Bottom Black plates (Thermo-Fisher) and equilibrated for 1 h in room temperature. After equilibration, GCaMP3 fluorescence was recorded using TECAN Infinite M200 Pro plate-reader, using excitation at 470 nm (7 nm bandwidth) and emission detection at 525nm (20nm bandwidth) with 20 μs integration time and 5 ms settle time. Absolute fluorescence values for each experiment were normalized to the untreated control value as F/F_{UT} (where F was the measured fluorescence at a given time point and F_{UT} was the averaged measurement for water-equilibrated uninfiltrated samples at each time points). Plotted values are averages of six replicate leaf discs, with the SE represented by error

bars. A similar protocol was used for semi-quantification of Ca^{2+} influx in Arabidopsis GCaMP6
plants(*57*). Plants were infiltrated with 10mM $MgCl_2$ with or without various *Pf0*-1 strains at
OD_{600nm} = 0.2. After 30 min of drying, 0.5cm leaf discs were gathered and equilibrated on water
for 30 min. Fluorescence was recorded every 10 min for 800 min. Blank values (water only)
5   were subtracted to sample values and calcium influx was expressed as F/F_0 , where F was the
measured fluorescence at a given time point and F_0 was the averaged measurement for $MgCl_2$-
infiltrated samples at this time points.

Ion leakage measurements:

10   Briefly, *A. tumefaciens* strains were infiltrated into *N. benthamiana* leaves and protein expression
induced as described above. 12 leaf discs (0.5 cm diameter) from 3 independent plants were
collected into clear tubes with 20 ml of distilled water and incubated at room temperature under
continuous light (three replicates per sample). Changes in conductivity were measured at the
indicated time points with an Orion Model 130 (Thermo-Fisher).

15

Human cell transfection:

Human cervical cancer cells (HeLa) or HEK293 were cultivated in DMEM medium containing
10% fetal bovine serum and 1% penicillin / streptomycin in a CO_2 incubator at 37C. Cells were
grown in 12-well plates overnight to 70-90% confluence and co-transfected with the "sleeping
20   beauty" pCMV(CAT)T7-SB100X vector containing the sleeping beauty transposase and the
pSBtet-Pur vectors - a gift from Long Ping V. Tse and Bill Marzluff - containing the synthesized,
human codon optimized, NRG1.1 constructs (Genescript) at a 1:10 ratio respectively.
GASDERMIN-D L192D N-terminal pore-forming domain (aa 1-275), a potent inducer of cell
death, and the loss of function GASDERMIN-D L192D DN5 were used as controls (*24, 58, 59*).
25   All constructs were YFP-tagged at the C-terminus. Briefly, for each co-transfection, 25μL of
Opti-MEM medium was mixed with 0.75uL of Lipofectamine 3000 (Invitrogen) in one tube
while 1μg of the plasmid mix was added to 25μL of Opti-MEM medium and 1uL of P3000
reagent in another tube. Solutions were mixed together and incubated at room temperature for 15
minutes before being added to the cell culture. After 2 days, puromycin 1μg.mL^{-1} (Sigma) was
30   added to the cultures to select transfected cells.

6

Protein assays:

Agrobacterium tumefaciens strains were infiltrated into *N. benthamiana* leaves as described above. The OD_{600} was adjusted to 0.1 (35S::P19) and 0.8 for NRG1.1 constructs. Induction was done 24 hours post infiltration using 100 µM β-estradiol (Sigma-Aldrich; St. Louis, USA) and 0.002% [v/v] Silwet L-77 by spraying. Tissues for protein assays were collected 6 h post induction.

Total protein extract was prepared by adding total protein buffer [100 mM Tris-Cl pH 7.5, 150 mM NaCl, 1% Triton X-100, 1 mM EDTA pH 8.0, 0.1% SDS, 10 mM dithiothreitol (DTT) and 1x Sigma plant protease inhibitor cocktail] to the homogenized tissue at a ratio of 5 uL per mg (FW) tissue. Lysate was cleared by centrifuge at 20,000 x g for 30 min at 4°C.

For microsomal fractionation, sucrose buffer [20mM Tris (pH 8), 0.33M sucrose, 1mM EDTA, 5mM DTT and 1x Sigma plant protease inhibitor cocktail] was added to the homogenized tissue at a ratio of 5 uL per mg (FW) tissue. The extract was centrifuged at 2,000 x g for 5 minutes at 4°C to remove debris. The resulting supernatant was transferred to a new tube and designated as total protein. Cytoplasmic fraction was prepared by harvesting the supernatant after spinning the total protein fraction at 20,000 x g for 1 h at 4°C. The total membrane fraction was prepared from the resulting pellet by resuspending in 200 uL of buffer B (Minute[TM] plasma membrane protein isolation kit, Invent Biotechnologies) and spinning at 7,800 x g for 15 min at 4°C. The pellet was designated as total membrane fraction. The supernatant was transferred to 2 mL Eppendorf tube and mixed with 1.6 mL cold PBS buffer mixed by vortexing and spun at 16,000 x g for 45 min at 4°C to pellet the plasma membrane fraction.

For blue native polyacrylamide gel electrophoresis, modified GTEN buffer (*60*) [10% glycerol, 100 mM Tris-Cl pH7.5, 1mM EDTA, 150mM NaCl, 5mM DTT, 0.5% n-dodecyl-B-D-maltoside (DDM) and 1x Sigma plant protease inhibitor cocktail] was added to the homogenized tissue at a ratio of 5 uL per mg (FW) tissue. Lysate was cleared by centrifuge at 20,000 x g for 30 min at 4°C. The supernatant was transferred to a new tube and mixed with 4x NativePAGE Sample buffer (Invitrogen).

For SDS-PAGE, proteins were mixed with 4x SDS-PAGE loading buffer and heated for 5 min at 95°C and resolved in 10% SDS-PAGE gels. Separated proteins were transferred to nitrocellulose membrane (GE Healthcare). For BN-PAGE, proteins were resolved in 3-12% and NativePAGE[TM] (Invitrogen) gels, respectively, then transferred to PVDF membrane using iBlot[TM] 2 gel transfer device according to the instructions from the manufacturer. Membranes were blocked with 5% non-fat milk TBST and probed with primary anti-GFP (Roche, Cat. #: 11814460001, 1:1000) and secondary HRP-conjugated anti-mouse antibody (R&D Systems, Cat. #: HAF007, 1:5000).

Cell death observation in human cells:

After 2 passages, cells were seeded on 8 well chamber slides (Nunc Lab-Tek 155411), and protein expression was induced by addition of doxycycline $1\mu g.mL^{-1}$ (PHR1145, Sigma). 6 hours after doxycycline addition, the cells incubated in incubation buffer (10 mM HEPES, 140 mM NaCl, and 2.5 mM CaCl2, pH 7.4) containing $1\mu g.mL^{-1}$ propidium iodide (PI) for 5 min and observed under a confocal microscope LSM710 AxioObserver (Zeiss), using the Plan-Apochromat 10X/0.45 M27 objective. YFP was excited using a 514 nm laser collecting emission between 520-559 nm; PI was excited using a 561 nm laser with an emission spectrum of 590-627 nm. Percentage of cell death was determined as the number of PI-positive cells amongst YFP positive cells.

Plasma membrane pore quantification with scanning electron microscopy:

Transfected cells were seeded on glass 12mm glass slides and grown overnight to 70-90% confluence. 6 hours after doxycycline treatment, the media was removed and cells were washed in PBS and fixed in 2.5% glutaraldehyde in 0.1M sodium cacodylate at room temperature for 30 minutes and stored for several days at 4°C. To better preserve the membrane structure, decrease shrinkage artefacts and reduce the metal coating thickness, the cells were post- fixed in 1% osmium tetroxide in 0.1M sodium cacodylate buffer for 15 minutes followed by subsequent treatment with 2% tannic acid in water for 15 minutes and 1% osmium tetroxide in water for 15 minutes (61). The coverslips were rinsed in deionized water prior to gradual dehydration with ethanol (30%, 50%, 75%, 100%, 100%) and critical point dried using carbon dioxide as the transitional solvent (Samdri-795 critical point dryer, Tousimis Research Corporation, Rockville,

8

MD). Coverslips were mounted on 13mm aluminum stubs using double-sided carbon adhesive and sputter coated with 3 nm of gold-palladium alloy (60 Au:40 Pd, Cressington Sputter Coater 208HR, model 8000-220, Ted Pella, Redding, CA). Images were taken using a Zeiss Supra 25 FESEM operating at 5 kV, using the InLens detector, 30μm aperture, and ~5 mm working distance (Carl Zeiss SMT Inc., Peabody, MA). Plasma membrane pores were observed at 200,000 X magnification. Two micrographs were taken per cell and at least 11 cells were observed per cell line. Experiment was performed twice with similar results.

Imaging of $[Ca^{2+}]_i$ in HeLa cells:

Transfected HeLa cells were seeded on eight-well chambered coverglasses (Nunc Lab-tek 155411) and grown overnight in a CO_2 incubator at $37^{\circ}C$. 6 to 8h post induction with 1 μg mL^{-1} doxycycline, a Fura-2-based Ca^{2+} imaging assay was performed as previously described (29). Cells were loaded with the Ca^{2+} sensitive dye Fura-2AM (5 μM; Sigma) and incubated in a low $[CaCl_2]$ standard buffer containing 130 mM NaCl, 3 mM KCl, 0.6 mM $MgCl_2$, 10 mM glucose, 10 mM HEPES, pH7.4 (adjusted with NaOH), and 0.1 mM $CaCl_2$ for 30 min. A 7.5 mM $CaCl_2$ standard buffer was added with a peristaltic pump (Dynamax RP-1, Rainin) to adjust final $[CaCl_2]$ to 2.5 mM. Fura-2 fluorescence imaging was performed using the Zeiss Axiovert 200 microscope equipped with two filter wheels (Lambda 10-3; Sutter Instruments) and a CMOS camera (Prime 95B sCMOS; Roper Scientific). Excitation was at 340 nm and 380 nm, and emission images at 510 nm were collected using the MetaFluor Fluorescence Ratio Imaging Software (Molecular Devices). Ratiometric (F340 nm/F380 nm) image data from 10 cells per well were analyzed. Experiments were carried out at room temperature (22–24°C). Delta ratio was found by calculating the difference of the average fluorescence ratio from 10 cells from 6 time points after switching to high $[CaCl_2]$ and those same cells at 6 time points before switching to high $[CaCl_2]$.

Imaging of $[Cl^-]_i$ in HeLa cells:

Transfected HeLa cells were seeded on eight-well chambered borosilicate cover glasses (Nunc Lab-tek 155411) and grown overnight. At 6 to 8h post induction with 1 μg mL^{-1} doxycycline, cells were subjected to a 6-Methoxy-N-ethylquinolinium iodide (MEQ) -based Cl$^-$ assay as previously described (33). DihydroMEQ was prepared freshly from MEQ. 5 mg of MEQ were

dissolved in 100 μL of distilled water. The MEQ solution was flushed with nitrogen and reduced to dihydroMEQ by addition of 32 μmol of sodium borohydride with continuous purging with nitrogen. DihydoMEQ was extracted with chloroform, dried with anhydrous sodium sulfate and the organic extracts were evaporated under a vacuum. DihydroMEQ was dissolved in DMSO

5   and added to a low chloride buffer (5 mM KCl, 20 mM HEPES, 90 mM mannitol) at a final concentration of approximately 50 μM. Cells were incubated for 5-10 minutes in the low chloride, dihydroMEQ containing buffer, rinsed and incubated 15 minutes in 200 μL of low chloride buffer before confocal observation. Basal MEQ fluorescence was imaged for 5 min before addition of 100 μL of 200 mM NaCl. Data was analyzed using FiJi (*56*). The MEQ

10   fluorescence of 12 cells was followed up in each experiment. Experiments were carried out at room temperature.

Mammalian cell electrophysiology:

HEK293 cells transfected with NRG1.1 DV or NRG1.1 DV D3N E14Q were seeded on glass

15   coverslip (12mm borosilicate, #1 thickness, Fisher scientific 12-545-80P), and ion channel activities were analyzed using the patch clamp electrophysiological technique as previously described (*28, 29, 62*). Whole-cell currents were recorded only on YFP-positive cells 4 to 8h after doxycycline induction. Pipettes (Kimax 51) were pulled in 2 to 3 steps using the P-1000 pipette puller and heat-polished to obtain $1–5$ MΩ resistance in the standard pipette solution (140

20   mM CsCl, 5 mM EGTA and 10 mM HEPES, pH 7.4 (adjusted with CsOH). Liquid junction potentials were measured as previously described and subtracted to the pipette voltage. Calcium and magnesium bath solutions consisted of 112 mM $CaCl_2$ or $MgCl_2$, 10mM glucose, and 10 mM HEPES (pH 7.4, adjusted with CaOH or MgOH). TEA-Cl bath solution consisted of 224 mM TEA-Cl, 10 mM glucose and 10 mM Tris (pH 7.4 adjusted with HCl). TEA-Cl pipette

25   solution contained 20 mM TEA-Cl, 5 mM EGTA and 10 mM Tris (pH 7.4, adjusted with HCl). Osmolality of all solutions were adjusted to 290 mOsm with sorbitol. Whole-cell voltage-clamp experiments were performed using the Axopatch 200B patch-clamp amplifier (Molecular Devices), and data were acquired using Digidata 1322A digitizer and the pClamp software. The whole-cell currents were recorded at room temperature with the holding potential at -50 mV and

30   the voltage ramp ranging from +50 to -200 mV in 1.9 s. No leak subtraction was performed. Permeability ratios for divalent cations to Cs^+ (P_X/P_{Cs}) were calculated as follows:

10

$P_X/P_{Cs} = [Cs^+]_i \exp(E_{rev}F/RT)(1+\exp(E_{rev}F/RT))/4[X^{2+}]_o$ where E_{rev} is the reversal potential (as measured from voltage ramp experiments), F is the Faraday's constant, R is the universal gas constant, and T is the absolute temperature. Brackets indicate ionic activities, and ion activity coefficients were 0.75 for Cs^+ and 0.25 for Ca^{2+} and Mg^{2+} (*28*).

Table S1 | Crystallography data collection and refinement statistics

	2K/E native	7K(R)/E native
PDB code	7L7W	7L7V
Wavelength (Å)	1.03316	1.03317
Resolution range (Å)	40.00 – 2.55 (2.59 – 2.55)	40.00 – 2.95 (3.00 – 2.95)
Space group	R 3 :H	P 2_1 2 2_1
a, b, c (Å)	114.257, 114.257, 59.855	84.332, 89.656, 149.398
α, β, γ (°)	90, 90, 120	90, 90, 90
Total reflections	78,469	289,192
Unique reflections	9,220 (338)	24,727 (1,218)
Multiplicity	8.5 (3.9)	11.7 (8.5)
Completeness (%)	96.2 (72.7)	99.8 (100.0)
I/σ(I)	27.2 (2.6)	18.4 (1.0)
Wilson B factor (Å^2)	57	54
R_{merge} (%)	10.5 (90.8)	13.0 (168.7)
R_{meas} (%)	11.1 (101.4)	13.5 (179.3)
R_{pim} (%)	3.6 (43.7)	3.9 (59.4)
$CC_{1/2}$	0.995 (0.692)	0.996 (0.506)
CC*	0.999 (0.904)	0.999 (0.820)
Refinement statistics		
Resolution (Å)	38.13 – 2.55 (2.64 – 2.55)	39.61 – 2.95 (3.03 – 2.95)
Reflections used in refinement	9,144 (658)	23,168 (1,670)
R_{cryst}	0.193 (0.314)	0.219 (0.340)
R_{free}	0.233 (0.419)	0.240 (0.362)
Number of non-hydrogen atoms	1,005	5,239
macromolecules	996	5,239
solvent	7	0
Protein residues	118	651
RMS bonds (Å)	0.0085	0.013
RMS angles (°)	1.096	1.628
Ramachandran Favored (%)	94.8	93.7
Ramachandran Allowed (%)	5.2	6.2
Ramachandran Outliers (%)	0	0.2
Rotamer outliers (%)	0	5.7
Clashscore	6.40	9.50

12

Average B-factor (Å^2)	73	94
macromolecules (Å^2)	73	94
solvent (Å^2)	58	N/A

Table S2: Proteins structurally similar to AtNRG1.1 2K/E, based on program Dali

PDB ID	Z-score	RMSD (Å)	Description
6j5v	10.0	2.3	Arabidopsis CC-NB-LRR ZAR1
4m70	9.4	2.4	Potato CC-NB-LRR Rx
4btf	9.3	2.4	Mouse MLKL
2ncg	8.8	2.8	Wheat CC-NB-LRR Sr33
6e7e	8.5	2.7	Inclusion membrane protein A
3rip	8.5	3.2	Ganna-tubulin complex component 4
3ay5	8.4	2.8	Cyclin-D1-binding protein 1
3zni	8.1	2.7	E3 Ubiquitin-protein Ligase CBL-B
1r0d	8.0	3.0	Huntingtin interacting protein 12
5y2g	7.9	3.5	Maltose-binding Periplasmic protein, protein B

Table S4: List of oligos used in this study

Oligos for cloning NRG1.1_1-180:GFP in pCSL86922	
Name	**Sequence**
OF298_ATNRG1_7_1-180-GSAForward	taGGTCTCtAatgaacgattgggctagtttgggaata
OF299_ATNRG1_8_1-180-GSAReverse	taGGTCTCtAGCAGATCCcttctttaactcccccaatggcca
OF304_GSAGFPForward	taGGTCTCtTGCTGGATCTGCTatggtgagcaagggcgagg
OF305_GSAGFPReverse	taGGTCTCtaagcctacttgtacagctcgtccatgcc
OF477_NRG1_17-180_F	taGGTCTCtAATGTTTTCCAAGCTCCTGAAAGTTGTGATTGA
Oligos for ADR1 N-terminal negative charge mutations	
Name	**Sequence**
ADR1_D6Ncttc69F	tataggtctcg**cttc**ATGGCTTCGTTCATA**aAT**CTTTTCGCCGGC**GAC**ATCACGAC
ADR1_D11Ncttc69F	tataggtctcg**cttc**ATGGCTTCGTTCATA**GAT**CTTTTCGCCGGC**caAC**ATCACGACGCAACTCTTAAAGCTGCT
ADR1_D611CTTC69F	tataggtctcg**cttc**ATGGCTTCGTTCATA**aAT**CTTTTCGCCGGC**aAC**ATCACGACGCAACTCTTAAAGCTGCT
ADR1a_GTCA69-R	tataggtctca**tGAC**CGTGACACAGTCAAAAACAAAACCTTA
ADR1b_GTCA69-F	tataggtctcg**gtca**CCGAATTTTGAGAATTTGGAGTCTTGTATA
ADR1b_GGAC69-R	tataggtctca**gtcc**CTCAAAACATCGTGTTGCGTCACAAATACA
ADR1c_GGAC69-F	tataggtctca**GGAC**CTAGCCCTTCATATGTCCAATCGTG
ADR1_CACC69-R	tataggtctca**ggtg**ATCGTCAAGCCAATCCACGGTGAAG
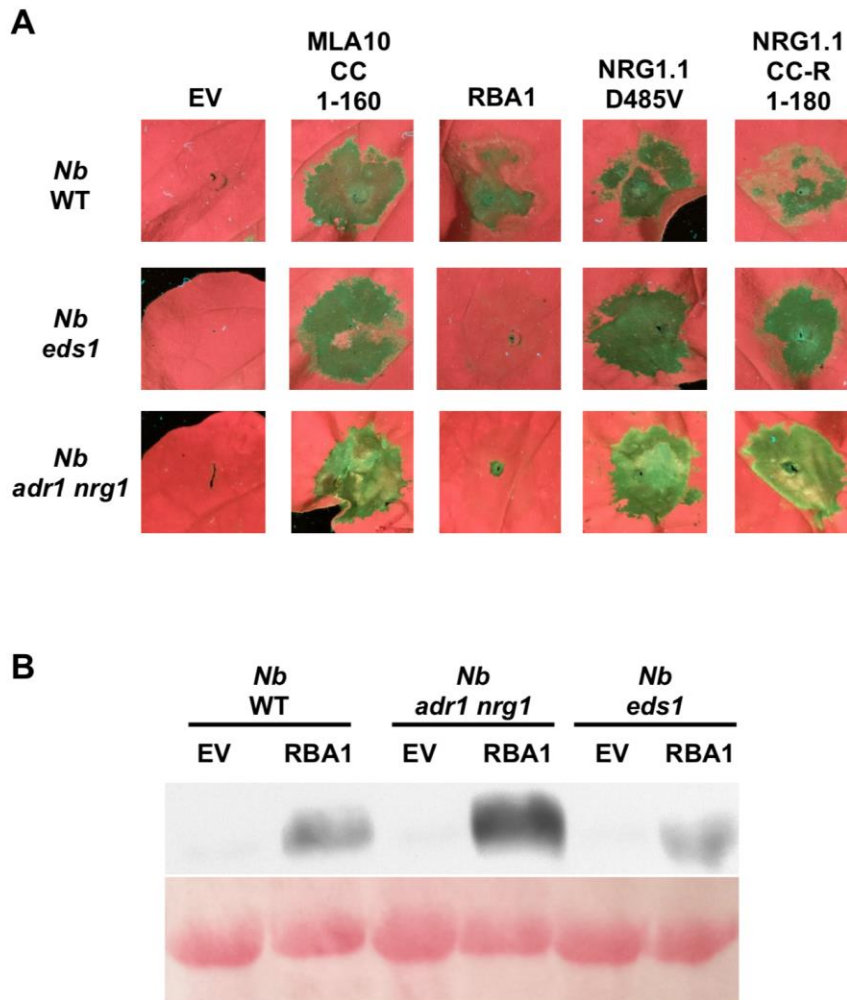
Fig. S1. Auto-active AtNRG1.1 D485V triggers cell death independently of EDS1 and NRG1/ADR1 in *Nb*.

(**A**) UV-image of *Nicotiana benthamiana (Nb)* leaves of indicated genotypes *Nb*, *Nb eds1* or *Nb adr1 nrg1* infiltrated with Agrobacterium harboring indicated Myc-tagged constructs to observe cell death phenotype 3 days post infiltration. A 180 aa N-terminal fragment of NRG1.1 is a control for cell death inductions (*63*). (**B**) Myc-tagged RBA1 proteins extracted from harvested leaf tissues 26 hours post infiltration were resolved by SDS-PAGE and blotted for Myc.
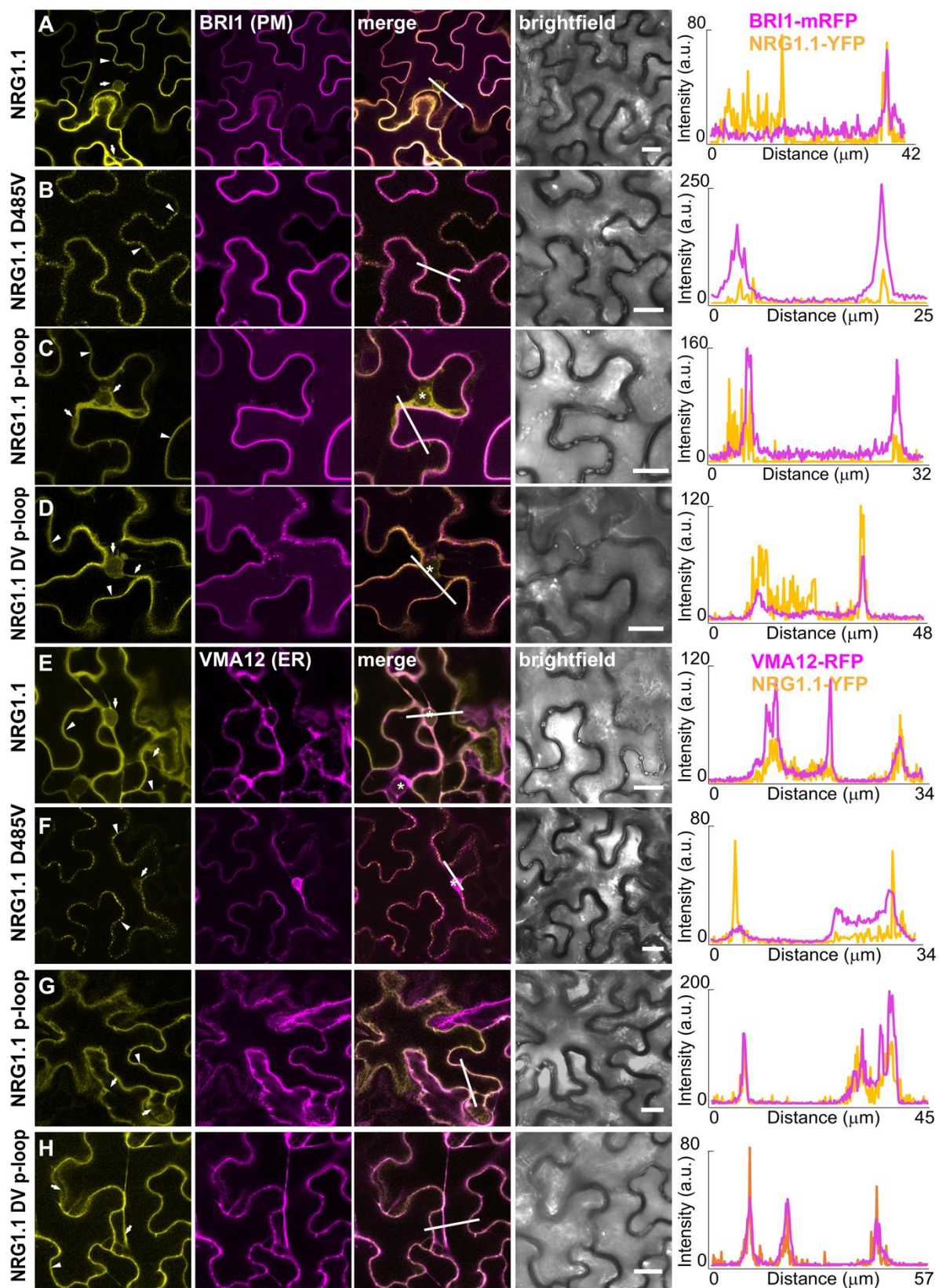
Fig. S2. Active NRG1.1 localizes to the plasma membrane. Continued.

17

Fig. S2. Active NRG1.1 localizes to the plasma membrane.

A to **D** are representative images showing the (co-)localization of wildtype NRG1.1 (**A**), NRG1.1 D485V (**B**), NRG1.1 p-loop (**C**) and NRG1.1 DV p-loop (**D**) with the plasma membrane (PM) localized BRI1-mRFP. **E** to **H** are representative images showing the (co-) localization of wildtype NRG1.1 (**E**), NRG1.1 D485V (**F**), NRG1.1 p-loop (**G**) and NRG1.1 DV p-loop (**H**) with the endoplasmic reticulum (ER) localized VMA12-RFP. Notably, active NRG1.1 D485V colocalizes poorly with VMA12 (ER) and strongly with BRI1 (PM) whereas the WT, inactive p-loop and DV p-loop colocalize strongly with the ER marker VMA12 and partially with the PM marker BRI1. Indicated proteins were transiently expressed in 4-6 week-old wildtype *Nicotiana benthamiana* plants. Expression of the indicated NRG1.1 constructs was induced 24 hours post infiltration with 20uM β-estradiol + 0.001% [v/v] Silwet L-77 and confocal imaging was performed 6 to 24 hours post induction. Arrowheads in **A** to **H** point to plasma membrane and/or punctate structure localization and arrows indicate endoplasmic reticulum localization. Lines in the merged images indicate the path of the intensity profile shown on the right and are pointing from left to right or up to down. Scale bars = 20 μm.
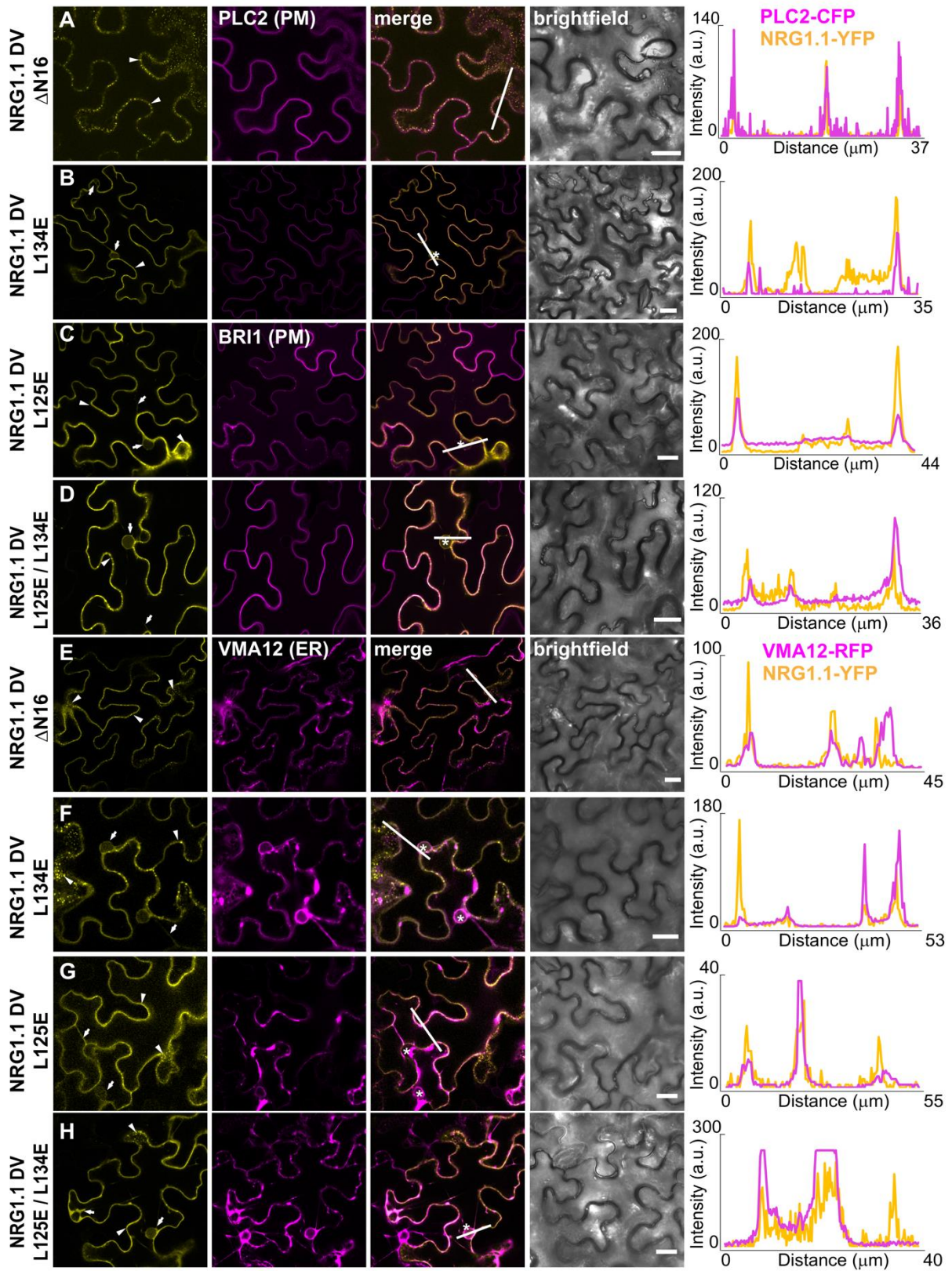
Fig. S3. Impact of structure-derived mutations on NRG1.1 localization. Continued.

Fig. S3. Impact of structure-derived mutations on NRG1.1 localization.

A to **D** are representative images showing the (co-) localization of NRG1.1 DV ΔN16 (**A**), NRG1.1 DV L134E (**B**), NRG1.1 DV L125E (**C**) and NRG1.1 DV L125E/L134E (**D**) with the plasma membrane (PM) localized BRI1-mRFP or PLC2-CFP, as indicated. **E** to **H** are representative images showing the (co-)localization of NRG1.1 DV ΔN16 (**E**), NRG1.1 DV L134E (**F**), NRG1.1 DV L125E (**G**) and NRG1.1 DV L125E/L134E (**H**) with the endoplasmic reticulum (ER) localized AtVMA12-RFP. Notably, NRG1.1 DV ΔN16 and NRG1.1 DV L125E colocalize strongly with the PM marker PLC2 or BRI1 and less so with the ER marker VMA12, whereas NRG1.1 DV L134E and NRG1.1 DV L134E/L125E colocalize strongly with the ER marker VMA12 and less so with the PM markers PLC2 or BRI1. Indicated proteins were transiently expressed in 4-6 week-old wildtype *Nicotiana benthamiana* plants. Expression of indicated NRG1.1 constructs was induced 24 hours post infiltration with 20uM β-estradiol + 0.001% [v/v] Silwet L-77 and confocal imaging was performed 6 to 24 hours post induction. Arrowheads in **A** to **H** point to plasma membrane and/or punctate structure localization and arrows indicate endoplasmic reticulum localization. Lines in the merged images indicate the path of the intensity profile shown on the right and are pointing from left to right or up to down. Scale bars = 20 μm.

20
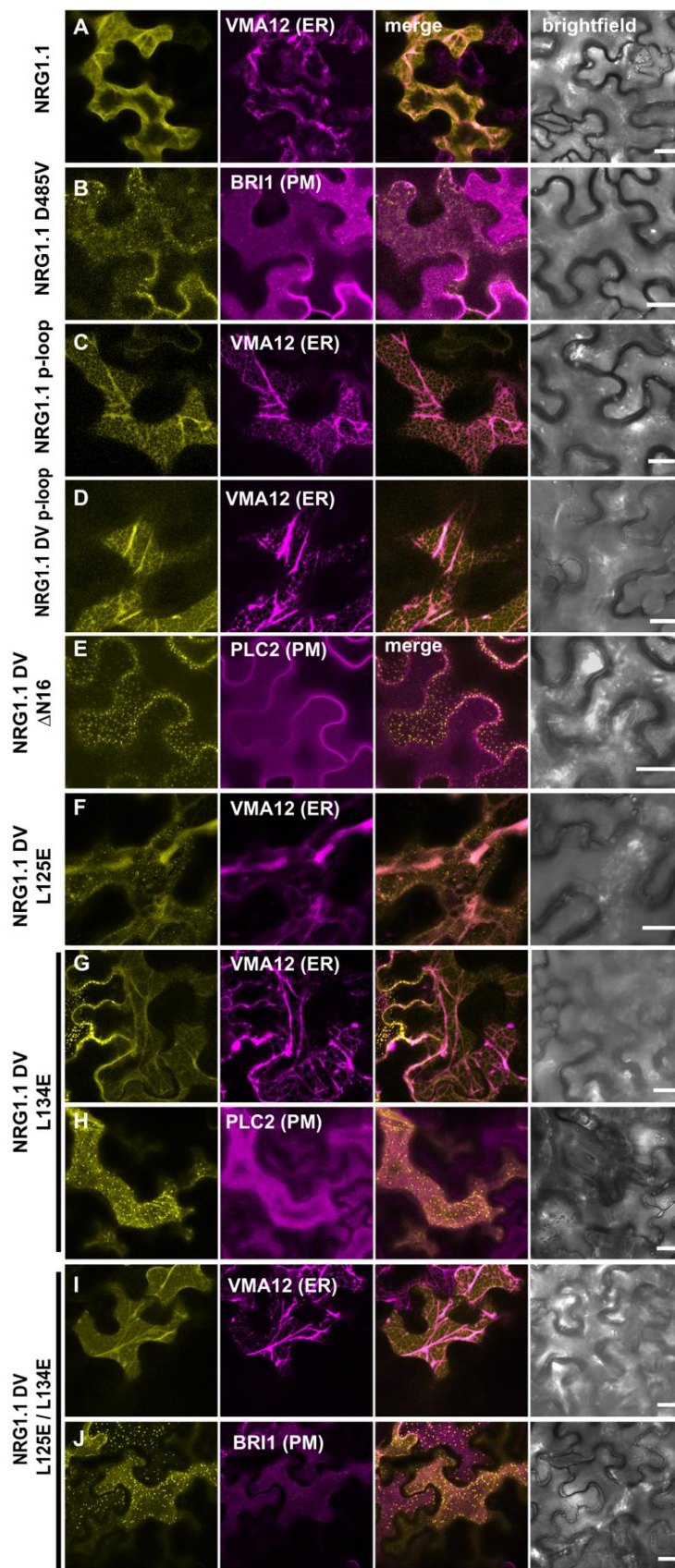
Fig. S4. Surface view of NRG1.1 WT and variants. Continued.

21

Fig. S4. Surface view of NRG1.1 WT and variants.

A to **J** are representative surface view images showing the (co-) localization of wildtype NRG1.1 (**A**), NRG1.1 D485V (**B**), NRG1.1 p-loop (**C**) and NRG1.1 DV p-loop (**D**), NRG1.1 DV ΔN16 (**E**), NRG1.1 DV L125E (**F**), NRG1.1 DV L134E (**G, H**) and NRG1.1 DV L125E/L134E (**I,J**) with either the plasma membrane (PM) localized AtBRI1-mRFP or AtPLC2-CFP or the endoplasmic reticulum (ER) localized AtVMA12-RFP. Importantly, PM localization is not uniform. PM localized NRG1.1 DV, NRG1.1 DV ΔN16 and NRG1.1 DV L134E were found in puncta at the PM whereas inactive NRG1.1 WT, p-loop and DV p-loop were associated with characteristic ER strands in some examples, NRG1.1 L134E and NRG1.1 DV L134E/L125E, to a much lesser extend NRG1.1 L125E, exhibited puncta at the PM which may reflect some residual PM localization (see also Fig 2C). Indicated proteins were transiently expressed in 4-6 week-old wildtype *Nicotiana benthamiana* plants. Expression of indicated NRG1.1 constructs was induced 24 hours post infiltration with 20uM β-estradiol + 0.001% [v/v] Silwet L-77 and confocal imaging was performed 6 to 24 hours post induction. Surface view images were constructed with the ImageJ software by combining 7-15 Z-stacks of the surface of individual cells into a maximum projection image. Note: For both the NRG1.1 DV L134E and NRG1.1 DV L125E/L134E mutants, we observed cells showing both strong ER localization (**G** and **I**) and the punctate localization pattern at the PM (**H** and **J**). Scale bars = 20 μm.
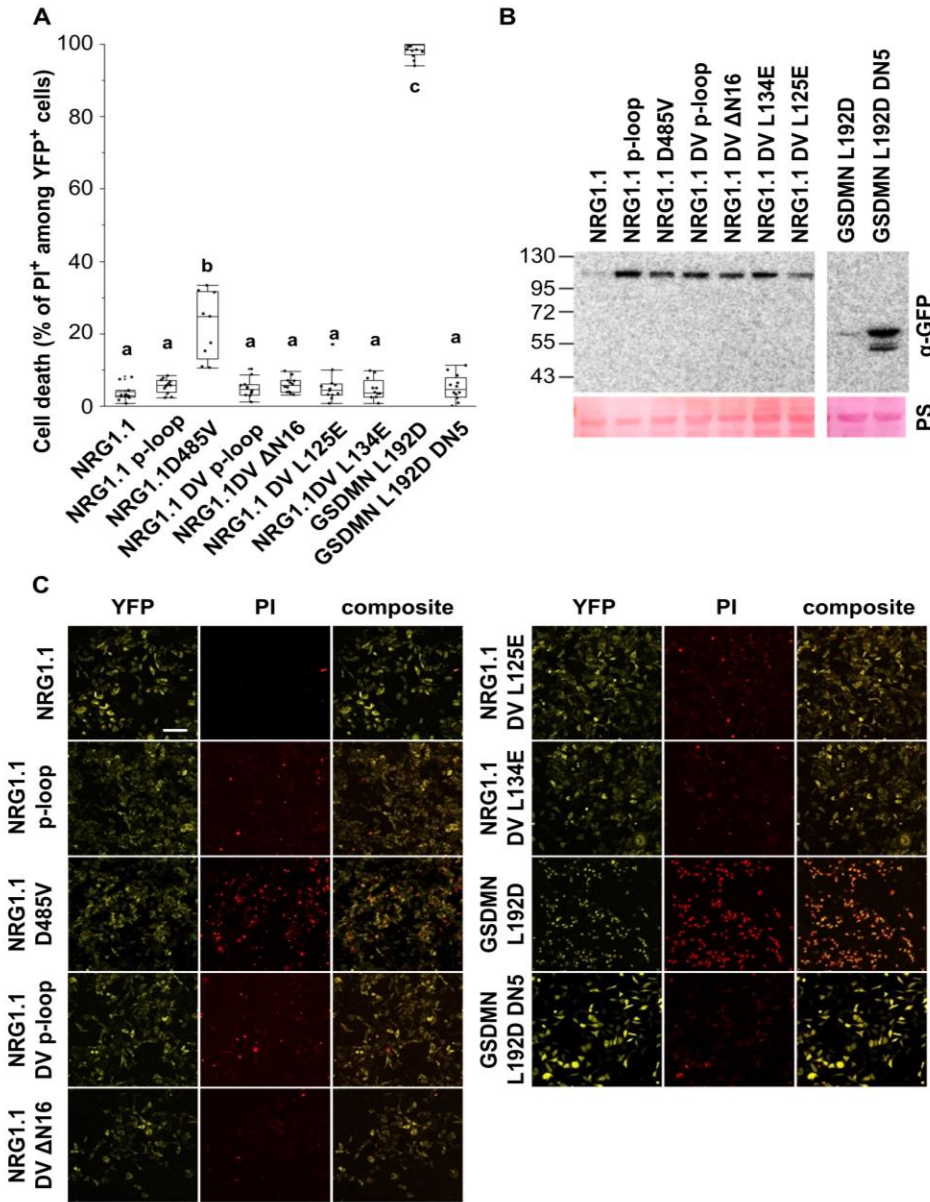
Fig. S5. NRG1.1 cell death induction function is conserved in HeLa cells. Continued.

Fig. S5. NRG1.1 cell death induction function is conserved in HeLa cells.

A Cell death percentage observed 6 hours post-induction (hpi) of protein expression with $1\mu g.ml^{-1}$ doxycycline. Cells were stained with propidium iodide (PI) and observed with a confocal microscope. The cell death is calculated as the percentage of PI^{+} cells among the YFP^{+} cells. Each data point is the average of counts from at least 3 different confocal images. The data presented here summarize 3 independent experiments. Letters represent statistical difference (ANOVA with post-hoc Tukey HSD test, p-value<0.0001). NRG1.1 cell death function can be recapitulated in HeLa cells. **B** Western blot confirming protein accumulation at 6hpi with doxycycline. Ponceau S stands for Ponceau Staining. **C** Representative confocal fluorescence images used for cell death quantification in **A**. Scale bar is 100μm.
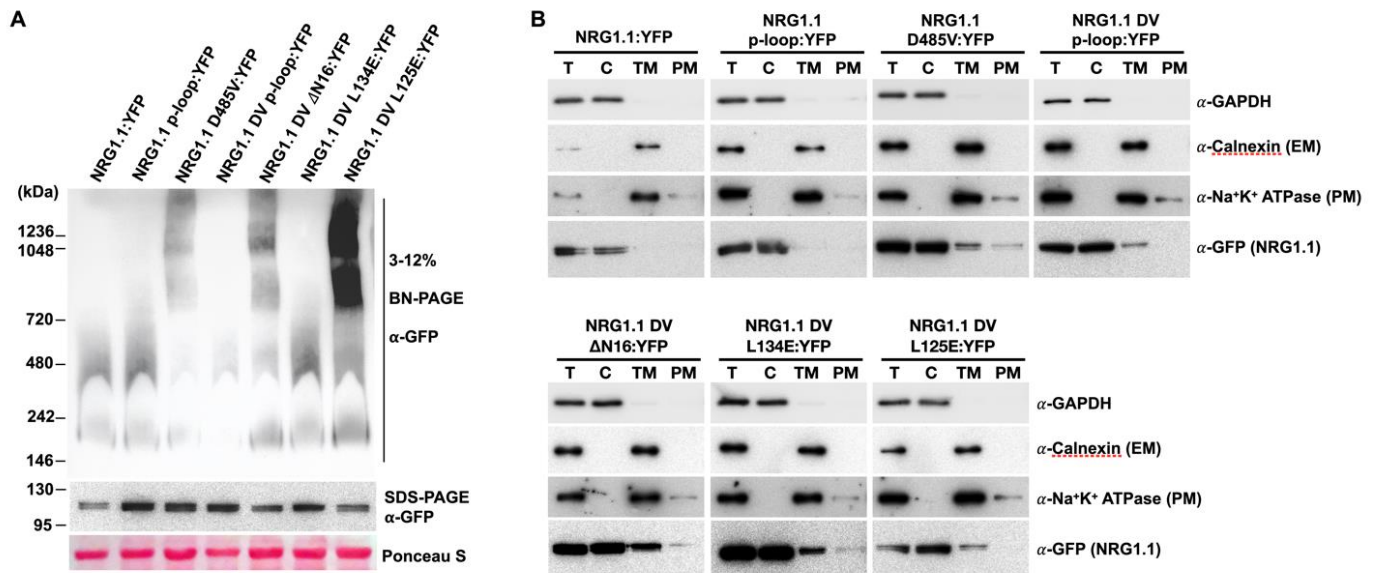
Fig. S6. Active NRG1.1 oligomerizes and localizes to the plasma membrane in HeLa cells.
A NRG1.1 DV forms high molecular weight oligomers in HeLa cells. Duplicate samples were analyzed by either SDS-PAGE (monomers) or BN-PAGE (oligomers). YFP tagged proteins were detected with anti-GFP antibody. Ponceau S stain is shown as loading control. **B** NRG1.1 localizes to the plasma membrane in HeLa cells. HeLa cells expressing indicated constructs were fractionated to Total proteins (T), cytosolic (C), total membrane (TM) and plasma membrane (PM) fractions and verified by marker proteins: Cytosol, GAPDH; endoplasmic reticulum membrane (EM), Calnexin;   PM, Na^+K^+ATPase. NRG1.1 proteins were detected by anti-GFP antibody.
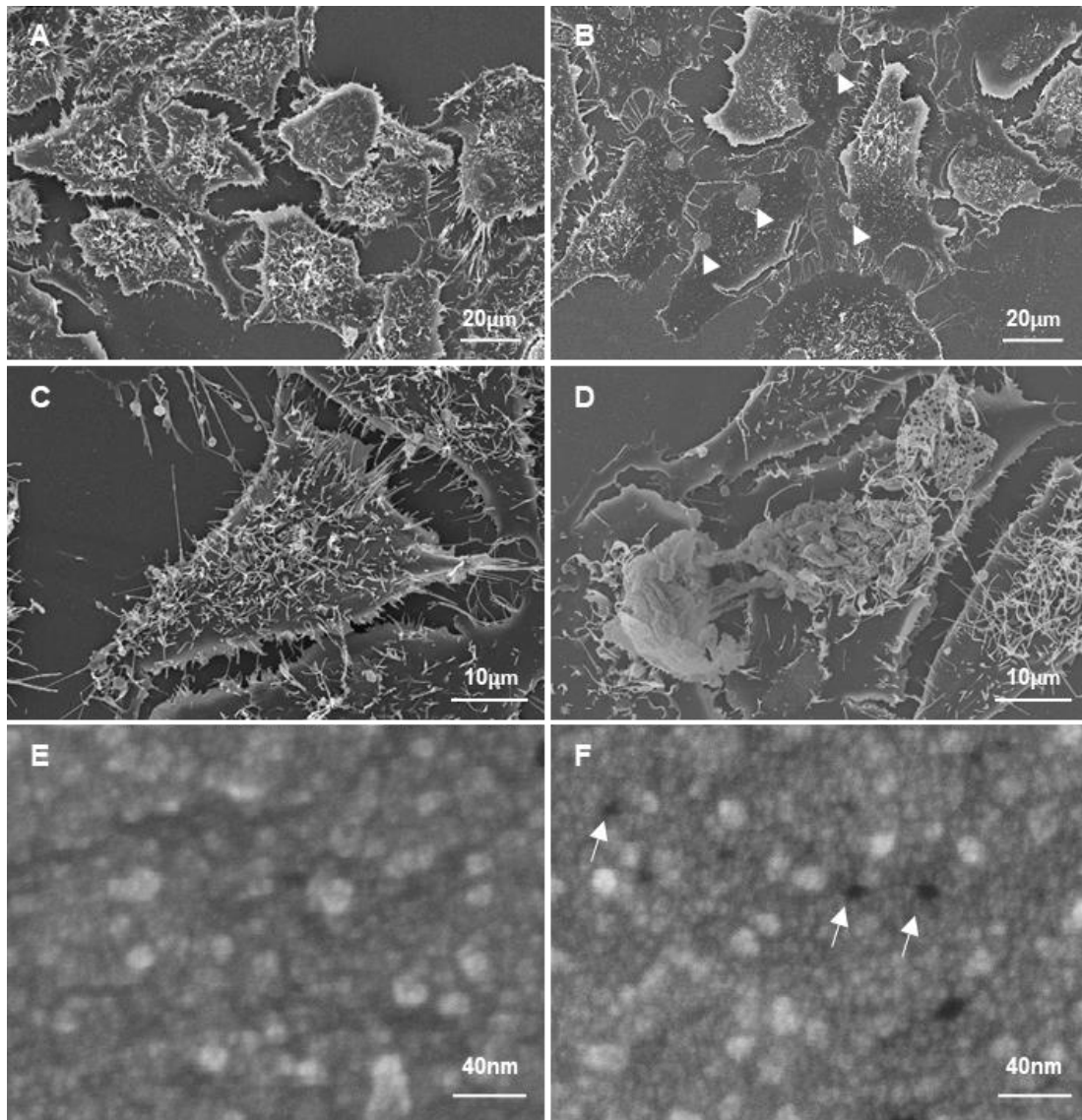
Fig. S7. Morphology of NRG1.1 D485V expressing cells.

Representative scanning electron microscopy pictures of HeLa cells 6 hours post doxycycline induction of inactive NRG1.1 D485V p-loop (**A**, **C** and **E**) or active NRG1.1 D485V (**B**, **D** and **F**). HeLa cells expressing the active NRG1.1 D485V (**B**) seem to have lost plasma membrane integrity and consequently appear flat with fewer microvilli compared to cells expressing the inactive NRG1.1 D485V p-loop (**A**). White arrowheads indicate large holes in the plasma membrane visible in many NRG1.1 D485V expressing cells. NRG1.1 D485V expressing cells occasionally showed "bubbling" reminiscent of pyroptosis (**D**). Expression of active NRG1.1 D485V was associated with a large number of plasma membrane pores (**F**) compared to the inactive control (**E**). White arrows indicate some plasma membrane pores.

26
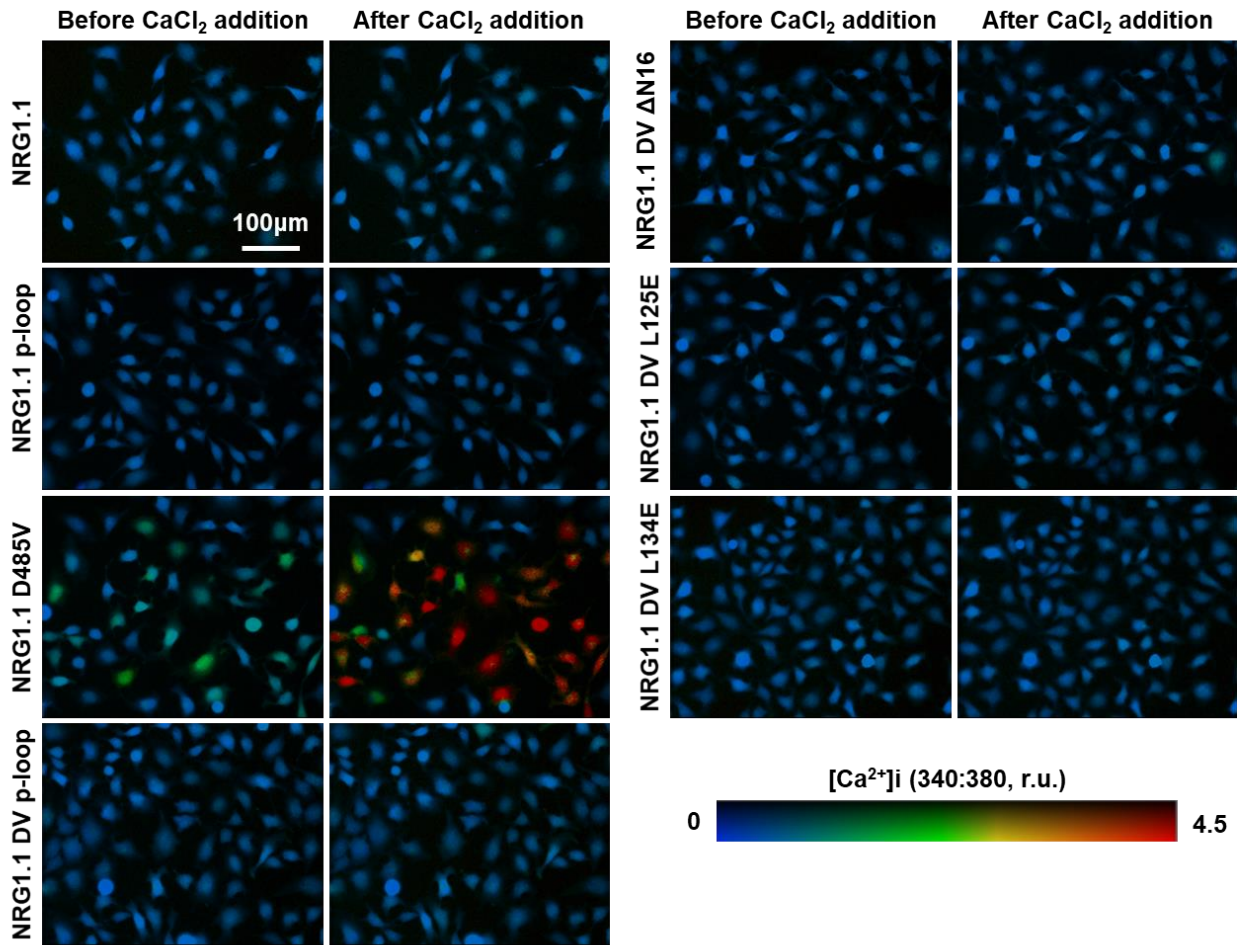
Fig. S8. Fura-2-based quantification of intracellular [Ca²⁺] in HeLa cells expressing NRG1.1 and variants.

Representative fluorescence microscopy images of HeLa cells expressing NRG1.1 WT or variant, as indicated, before or 2 minutes after 2.5mM $CaCl_2$ addition. Intracellular $[Ca^{2+}]$ was calculated from Fura-2 emission ratios (340:380 nm) and scaled using a pseudo-color bar. The ratios were quantified in Fig 3K.
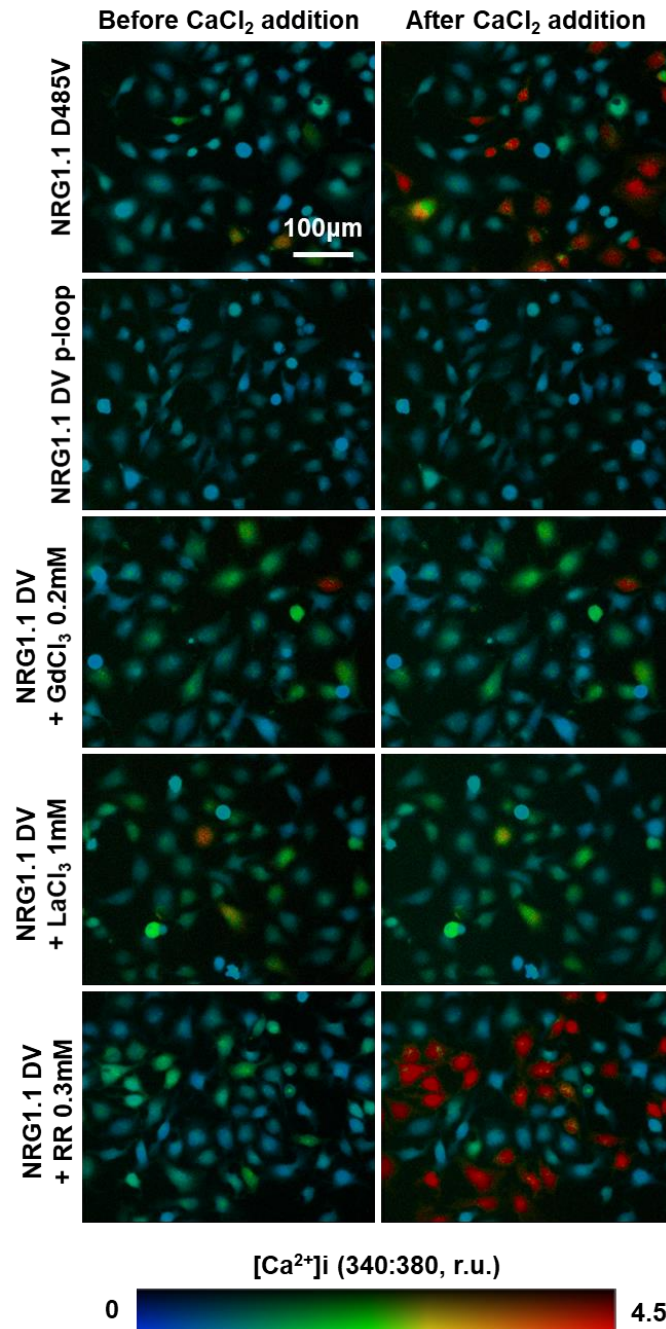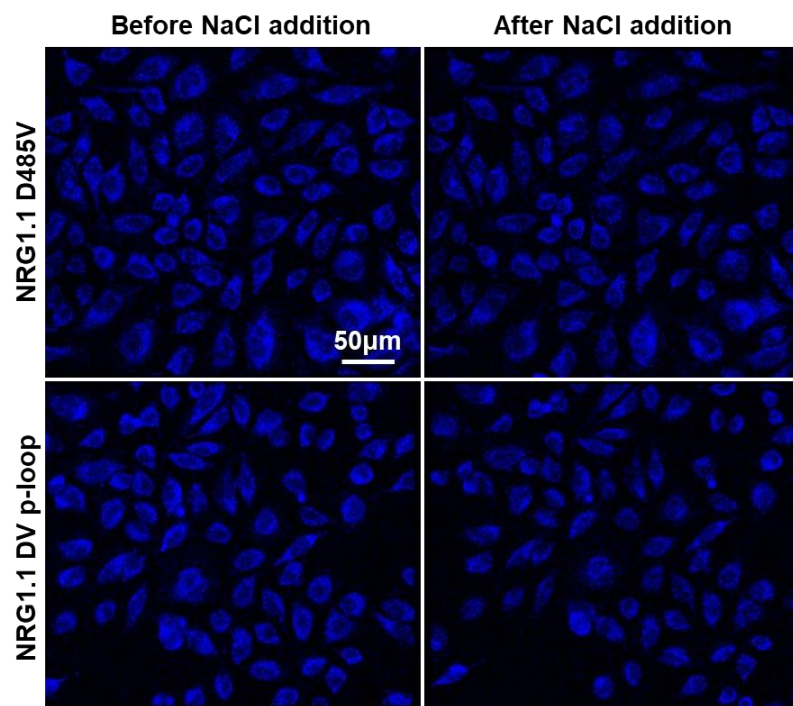
Fig. S9. Fura-2-based quantification of Calcium channel blockers impact on intracellular [Ca²⁺] in NRG1.1 D485V-expressing HeLa cells.

Representative fluorescence microscopy images of HeLa cells expressing active NRG1.1 D485V in the presence of typical calcium channel blockers, before or 2 minutes after 2.5 mM CaCl₂ addition. Intracellular [Ca²⁺] was calculated from Fura-2 emission ratios (340:380 nm) and scaled using a pseudo-color bar. The ratios were quantified in Fig3 L.

Before NaCl addition   **After NaCl addition**

NRG1.1 D485V

50µm

NRG1.1 DV p-loop

Fig. S10. MEQ-based quantification of intracellular [Cl⁻] in NRG1.1 D485V and NRG1.1 DV p-loop-expressing HeLa cells.

Representative fluorescence microscopy images of HeLa cells expressing active NRG1.1 D485V or suppressed NRG1.1 DV p-loop, before or 2 minutes after 200 mM NaCl addition. Intracellular [Cl⁻] was visualized from MEQ fluorescence quenching (emission at 440nm). The signal was quantified in Fig3 M.
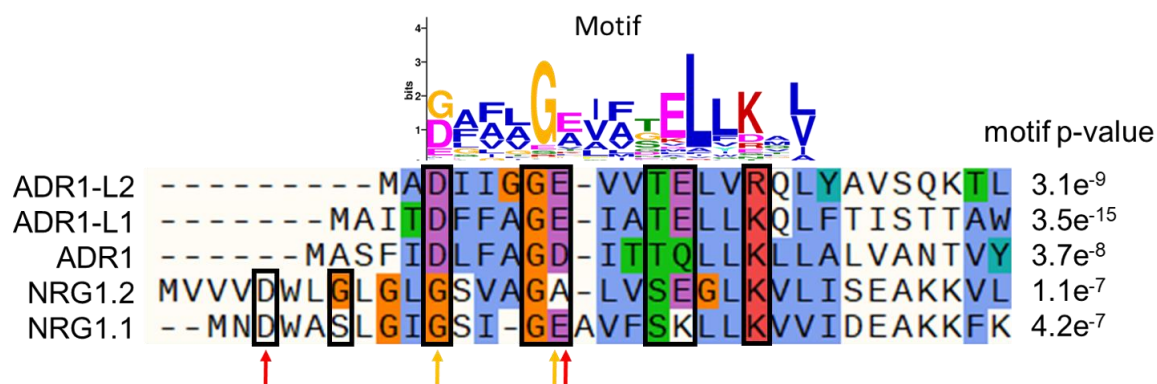
Fig. S11. The RNL N-terminal motif aligned to Arabidopsis ADR1s and NRG1s N-termini.
De novo motif discovery algorithm (MEME, meme-suite.org, (*64*)) run on 334 RNL N-terminal sequences (pfam.xfam.org; Table S3) allowed the identification of a conserved pattern of charged, polar or glycines residues (black boxes) separated by 2 to 3 hydrophobic residues (Motif E-value = 2.8e-1139, 331 occurrences). The motif is partially degenerated in NRG1.1 and NRG1.2 with K19 (NRG1.1) and A17 (NRG1.2) replacing E residues. Interestingly, NRG1.1 and NRG1.2 possess an N-terminal extension comprising D-G/S residues that seem to follow the same spacing pattern. Red and orange arrows indicate the residues that were mutated in NRG1.1 and ADR1 respectively.

E.value	Protein name
	Top Motif
2.80E-09	AtADR1-L1.1
2.80E-09	AtADR1-L1.2
9.40E-09	NbS00036756g0009.1
3.70E-06	Solyc04g079420
0.0016	Solyc02g090380
0.0025	AtADR1-L2
0.0066	NbNRG1
0.028	AtADR1
0.089	AtNRG1.1
0.34	AtNRG1.2
0.69	HORVU7Hr1G116000.1
0.97	HORVU3Hr1G109680.6
1.1	HORVU5Hr1G001020.2
1.2	NbS00012490g0007.1
2.3	HORVU5Hr1G078100.19
6.1	Os10g33440.2
6.4	Bv4_091520_ohgj.t1
6.4	HORVU5Hr1G085920.2
6.4	HORVU5Hr1G085940.2
7.5	Os10g07400.1
7.5	Os10g07400.2
9.4	Solyc11g069620
9.8	Bv3_063870_jjky.t1
9.9	Solyc10g055050
9.9	NbS00016761g0012.1

Fig. S12. The RNL N-terminal motif is not shared by CNLs.

The RNL N-terminal motif was used to scan (MAST, meme-suite.org, (*65*)) a database comprising 988 putative CC-NLRs and CC_R-NLRs from six representative plant species (Arabidopsis, sugar beet, tomato, N. benthamiana, rice and barley) from (*34*). The top 10 motif-containing protein were all RNLs and CNLs exhibited only a very degenerated version of the motif.
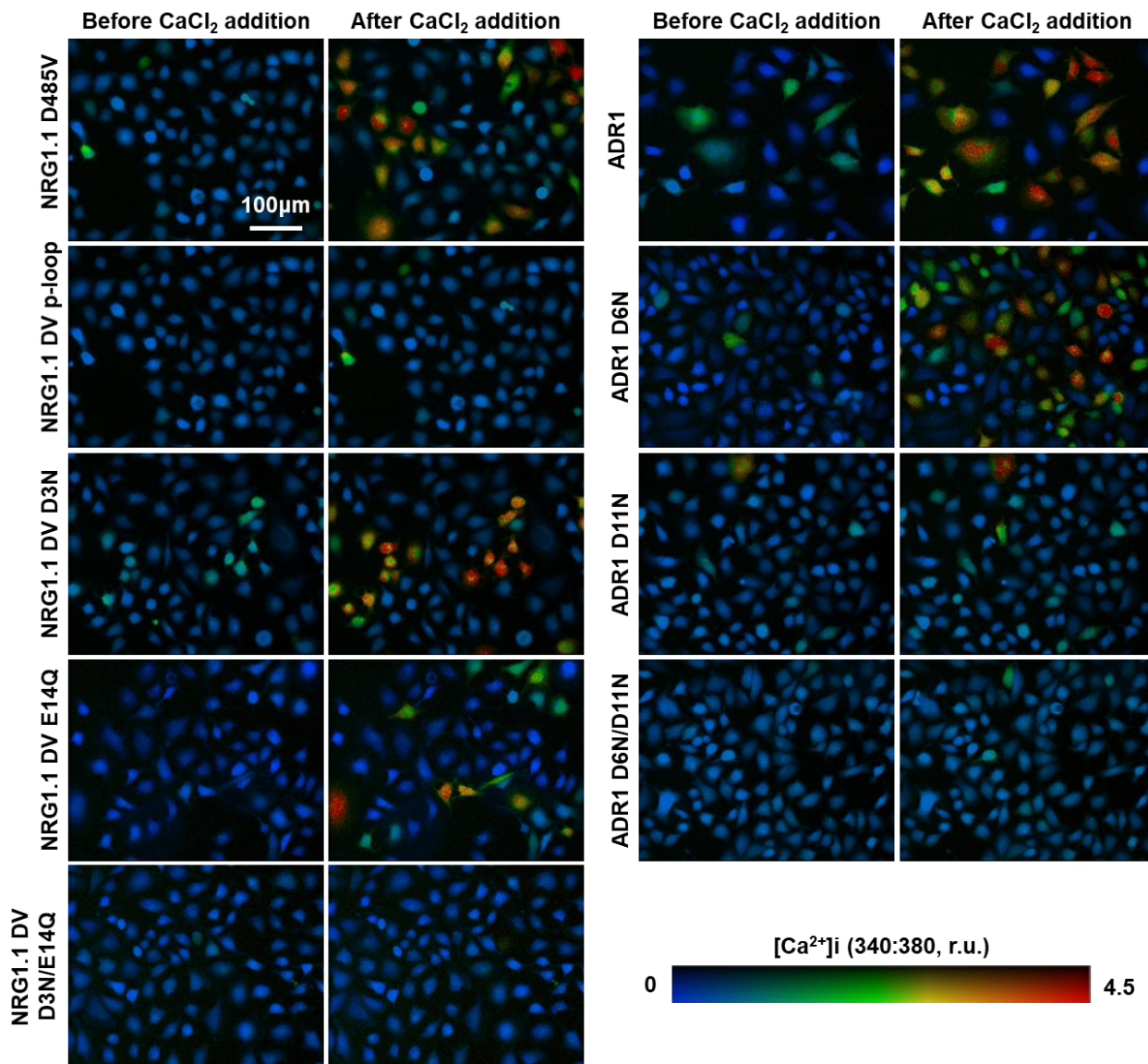
Fig. S13. Impact of mutation in the N-terminal RNL motif on intracellular $[Ca^{2+}]$ in NRG1.1 D485V and ADR1-expressing HeLa cells, as visualized with Fura-2.

Representative fluorescence microscopy images of HeLa cells expressing active NRG1.1 D485V, ADR1 or variants, before or 2 minutes after 2.5mM $CaCl_2$ addition. Intracellular $[Ca^{2+}]$ was calculated from Fura-2 emission ratios (340:380 nm) and scaled using a pseudo-color bar. The ratios were quantified in Fig4 H and J.
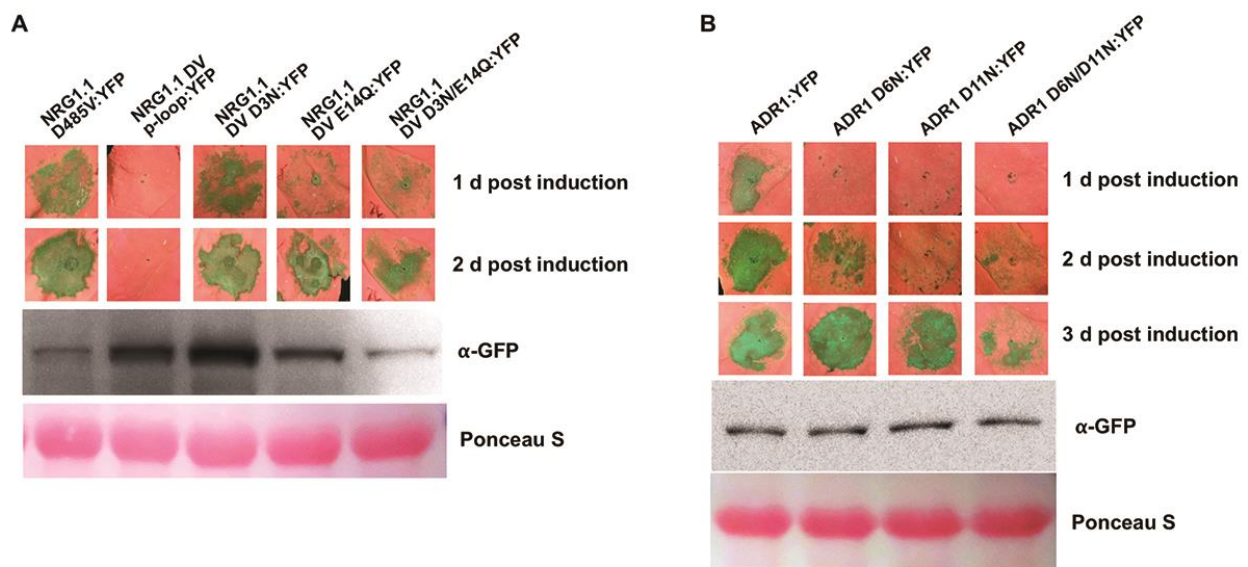
Fig. S14. Mutation of N-terminal negatively charged residues in NRG1.1 and ADR1 delays cell death in *Nicotiana benthamiana*

UV-image of *Nb* leaves infiltrated with Agrobacterium harboring indicated constructs to observe cell death phenotypes. YFP tagged NRG1.1 and ADR1 proteins extracted from harvested tissues 6 hours post induction were resolved by SDS-PAGE and blotted with anti-GFP antibody.
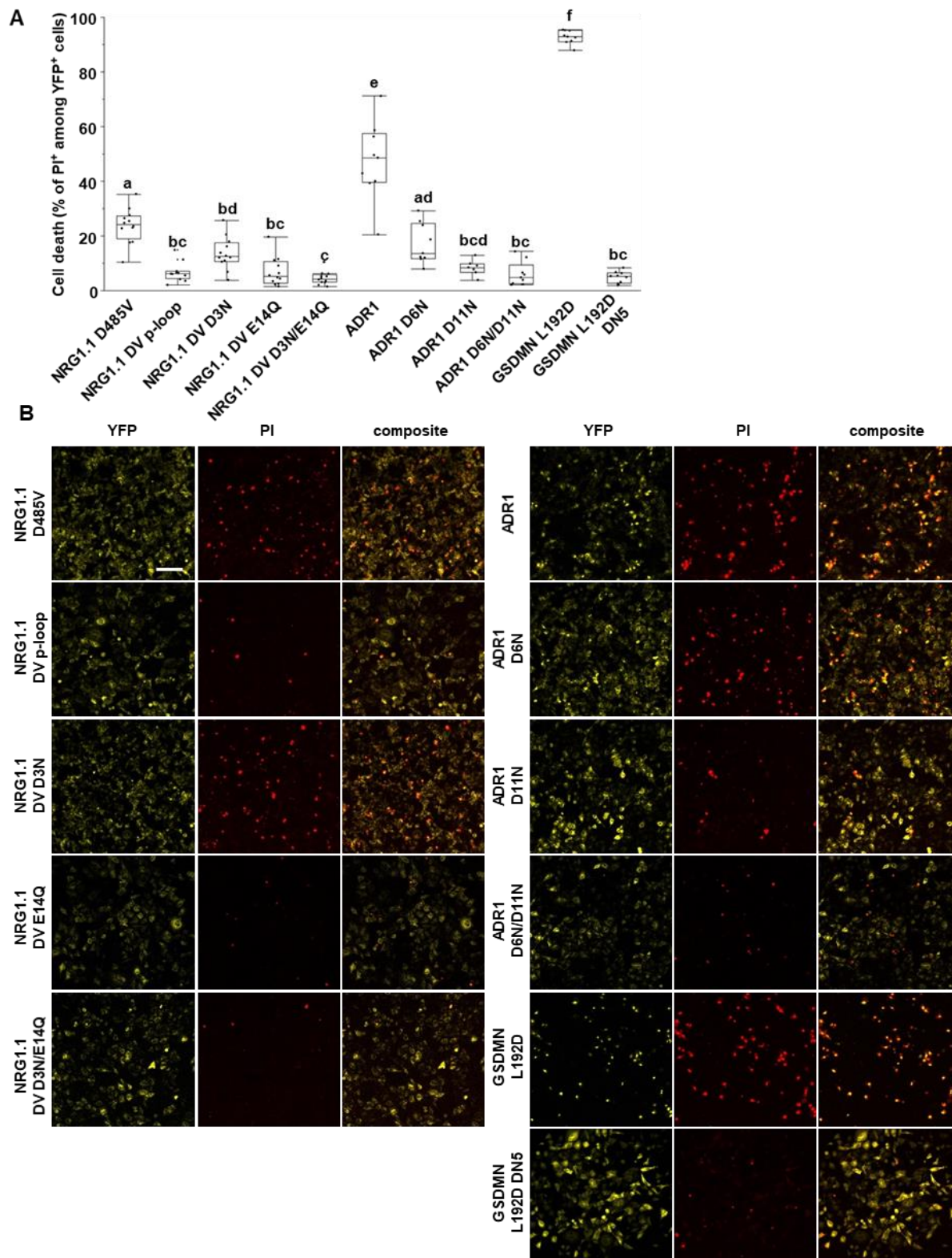
Fig. S15. Negatively charged residues in the conserved RNL N-terminal motif are required for cell death in HeLa cells. Continued.

Fig. S15. Negatively charged residues in the conserved RNL N-terminal motif are required for cell death in HeLa cells.

A Cell death percentage observed 6 hours post-induction (hpi) of protein expression with 1μg.ml^{-1} doxycycline. Cells were stained with propidium iodide (PI) and observed with a confocal microscope. The cell death is the percentage of PI^{+} cells among the YFP^{+} cells. The data presented here comes from 3 independent experiments. Letters represent statistical difference (ANOVA with post-hoc Tukey HSD test, p-value<0.05). **B** Representative fluorescence images used for cell death quantification in A. Scale bar is 100μm.

5

35
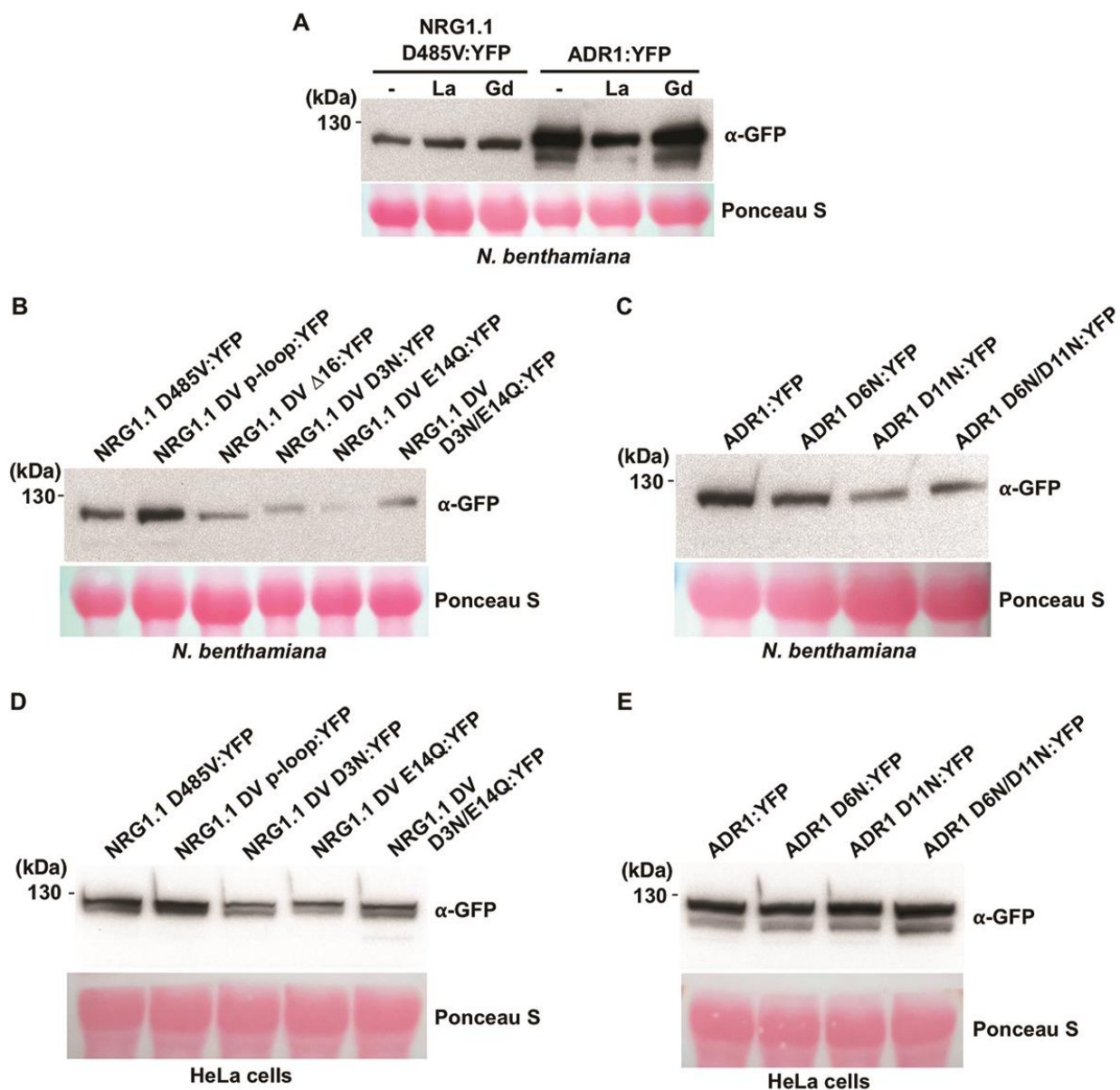
Fig. S16. RNL proteins are correctly expressed in *N. benthamiana* and HeLa cells.
Total proteins extracted from samples of Fig. 4B (**A**), Fig. 4C and 4D (**B**), Fig. 4E and 4F (**C**), Fig. 4G and 4H (**D**), and Fig. 4I and 4J (**E**) were resolved in 8% SDS-PAGE gel and transferred to nitrocellulose membranes. The RNL proteins were detected by immunoblotting the membranes with anti-GFP antibody.
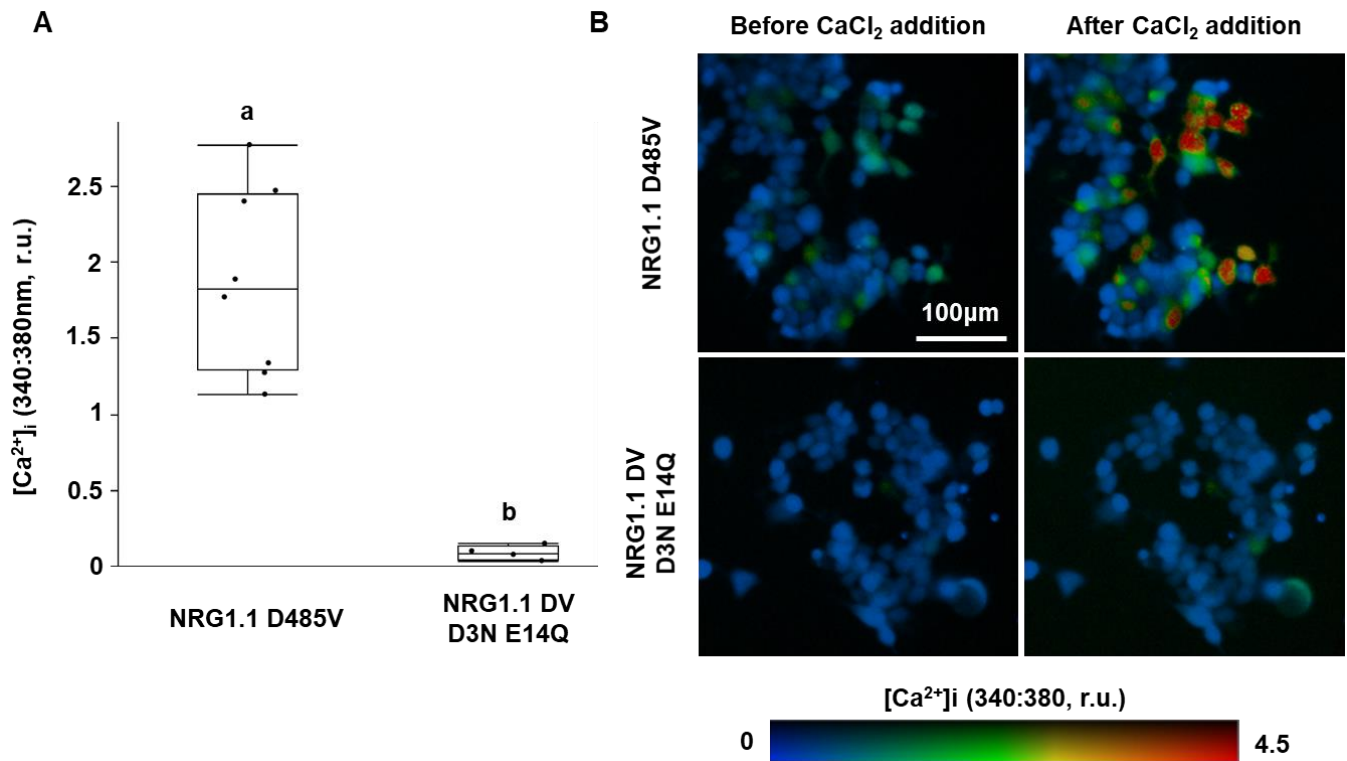
Fig. S17. NRG1.1 D485V triggers cytoplasmic Ca²⁺ influx in HEK293 cells.

(**A**) Intracellular [Ca²⁺] in HEK293 cells expressing active NRG1.1 D485V or NRG1.1 DV D3N E14Q loss of function mutant, before or 2 minutes after 2.5mM $CaCl_2$ addition. Intracellular [Ca²⁺] was calculated from Fura-2 emission ratios (340:380 nm) and scaled using a pseudo-color bar. Letters represent statistical difference (ANOVA with post-hoc Tukey HSD test, $p < 0.05$).

(**B**) Representative fluorescence microscopy images of HEK293 cells in (**A**).
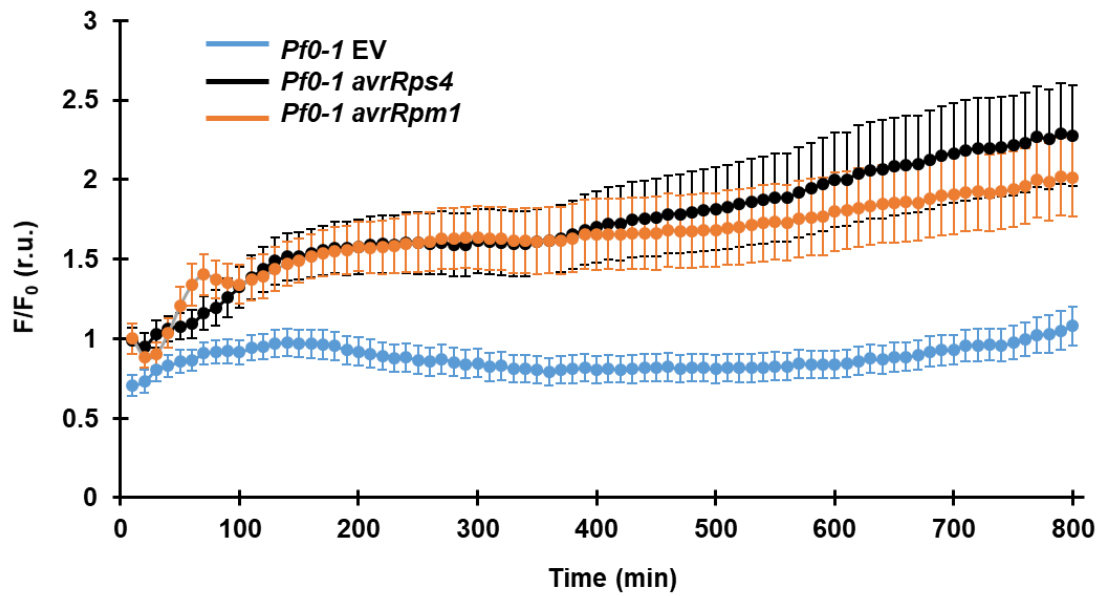
Fig. S18. Effector triggered RNL-dependent RPS4 TNL activity is associated with elevated cytoplasmic [Ca^{2+}].

Representative time course measurement of intracellular [Ca^{2+}]. *Arabidopsis* plants carrying the intracellular Ca^{2+} sensor GCaMP6 (*57*) were infiltrated with *Pseudomonas fluorescens 0–1* (*Pf0-1*, a *Pseudomonas* strain naturally devoid of type 3 secretion system that was engineered to express a *P. syringae* type 3 secretion system and deliver effectors (*66*)), carrying empty vector (EV), *avrRps4* or *avrRpm1* effector genes, as indicated. Error bars represent s.e.m (N = 16). The experiment was performed three times with similar results.

References and Notes

1. J. D. Jones, R. E. Vance, J. L. Dangl, Intracellular innate immune surveillance devices in plants and animals. *Science* **354**, aaf6395 (2016). doi:10.1126/science.aaf6395 Medline

2. B. Laflamme, M. M. Dillon, A. Martel, R. N. D. Almeida, D. Desveaux, D. S. Guttman, The pan-genome effector-triggered immunity landscape of a host-pathogen interaction. *Science* **367**, 763–768 (2020). doi:10.1126/science.aax4079 Medline

3. J. Tamborski, K. V. Krasileva, Evolution of plant NLRs: From natural history to precise modifications. *Annu. Rev. Plant Biol.* **71**, 355–378 (2020). doi:10.1146/annurev-arplant-081519-035901 Medline

4. I. M. L. Saur, R. Panstruga, P. Schulze-Lefert, NOD-like receptor-mediated plant immunity: From structure to cell death. *Nat. Rev. Immunol.* **21**, 305–318 (2020). doi:10.1038/s41577-020-00473-z Medline

5. S. C. Saile, P. Jacob, B. Castel, L. M. Jubic, I. Salas-Gonzáles, M. Bäcker, J. D. G. Jones, J. L. Dangl, F. El Kasmi, Two unequally redundant "helper" immune receptor families mediate *Arabidopsis* thaliana intracellular "sensor" immune receptor functions. *PLOS Biol.* **18**, e3000783 (2020). doi:10.1371/journal.pbio.3000783 Medline

6. L. M. Jubic, S. Saile, O. J. Furzer, F. El Kasmi, J. L. Dangl, Help wanted: Helper NLRs and plant immune responses. *Curr. Opin. Plant Biol.* **50**, 82–94 (2019). doi:10.1016/j.pbi.2019.03.013 Medline

7. D. Lapin, D. D. Bhandari, J. E. Parker, Origins and immunity networking functions of EDS1 family proteins. *Annu. Rev. Phytopathol.* **58**, 253–276 (2020). doi:10.1146/annurev-phyto-010820-012840 Medline

8. C. Van Ghelder, G. J. Parent, P. Rigault, J. Prunier, I. Giguère, S. Caron, J. Stival Sena, A. Deslauriers, J. Bousquet, D. Esmenjaud, J. MacKay, The large repertoire of conifer NLR resistance genes includes drought responsive and highly diversified RNLs. *Sci. Rep.* **9**, 11614 (2019). doi:10.1038/s41598-019-47950-7 Medline

9. D. T. N. Tran, E.-H. Chung, A. Habring-Müller, M. Demar, R. Schwab, J. L. Dangl, D. Weigel, E. Chae, Activation of a plant NLR complex through heteromeric association with an autoimmune risk variant of another NLR. *Curr. Biol.* **27**, 1148–1160 (2017). doi:10.1016/j.cub.2017.03.018 Medline

10. Z. Wu, M. Li, O. X. Dong, S. Xia, W. Liang, Y. Bao, G. Wasteneys, X. Li, Differential regulation of TNL-mediated immune signaling by redundant helper CNLs. *New Phytol.* **222**, 938–953 (2019). doi:10.1111/nph.15665 Medline

11. S. J. Williams, P. Sornaraj, E. deCourcy-Ireland, R. I. Menz, B. Kobe, J. G. Ellis, P. N. Dodds, P. A. Anderson, An autoactive mutant of the M flax rust resistance protein has a preference for binding ATP, whereas wild-type M protein binds ADP. *Mol. Plant Microbe Interact.* **24**, 897–906 (2011). doi:10.1094/MPMI-03-11-0052 Medline

12. W. I. L. Tameling, J. H. Vossen, M. Albrecht, T. Lengauer, J. A. Berden, M. A. Haring, B. J. C. Cornelissen, F. L. W. Takken, Mutations in the NB-ARC domain of I-2 that impair ATP hydrolysis cause autoactivation. *Plant Physiol.* **140**, 1233–1245 (2006). doi:10.1104/pp.105.073510 Medline

39

13. T. Qi, K. Seong, D. P. T. Thomazella, J. R. Kim, J. Pham, E. Seo, M.-J. Cho, A. Schultink, B. J. Staskawicz, NRG1 functions downstream of EDS1 to regulate TIR-NLR-mediated plant immunity in *Nicotiana benthamiana*. *Proc. Natl. Acad. Sci. U.S.A.* **115**, E10979–E10987 (2018). doi:10.1073/pnas.1814856115 Medline

14. D. Lapin, V. Kovacova, X. Sun, J. A. Dongus, D. Bhandari, P. von Born, J. Bautor, N. Guarneri, J. Rzemieniewski, J. Stuttmann, A. Beyer, J. E. Parker, A coevolved EDS1-SAG101-NRG1 module mediates cell death signaling by TIR-domain immune receptors. *Plant Cell* **31**, 2430–2455 (2019). doi:10.1105/tpc.19.00118 Medline

15. A. R. Bentham, R. Zdrzalek, J. C. De la Concepcion, M. J. Banfield, Uncoiling CNLs: Structure/function approaches to understanding CC domain function in plant NLRs. *Plant Cell Physiol.* **59**, 2398–2408 (2018). doi:10.1093/pcp/pcy185 Medline

16. A. Daskalov, B. Habenstein, R. Sabaté, M. Berbon, D. Martinez, S. Chaignepain, B. Coulary-Salin, K. Hofmann, A. Loquet, S. J. Saupe, Identification of a novel cell death-inducing domain reveals that fungal amyloid-controlled programmed cell death is related to necroptosis. *Proc. Natl. Acad. Sci. U.S.A.* **113**, 2720–2725 (2016). doi:10.1073/pnas.1522361113 Medline

17. J. Wang, M. Hu, J. Wang, J. Qi, Z. Han, G. Wang, Y. Qi, H.-W. Wang, J.-M. Zhou, J. Chai, Reconstitution and structure of a plant NLR resistosome conferring immunity. *Science* **364**, eaav5870 (2019). doi:10.1126/science.aav5870 Medline

18. B. Xia, S. Fang, X. Chen, H. Hu, P. Chen, H. Wang, Z. Gao, MLKL forms cation channels. *Cell Res.* **26**, 517–528 (2016). doi:10.1038/cr.2016.26 Medline

19. Z. Cai, S. Jitkaew, J. Zhao, H.-C. Chiang, S. Choksi, J. Liu, Y. Ward, L. G. Wu, Z.-G. Liu, Plasma membrane translocation of trimerized MLKL protein is required for TNF-induced necroptosis. *Nat. Cell Biol.* **16**, 55–65 (2014). doi:10.1038/ncb2883 Medline

20. J. Wang, J. Wang, M. Hu, S. Wu, J. Qi, G. Wang, Z. Han, Y. Qi, N. Gao, H.-W. Wang, J.-M. Zhou, J. Chai, Ligand-triggered allosteric ADP release primes a plant NLR complex. *Science* **364**, eaav5868 (2019). doi:10.1126/science.aav5868 Medline

21. G. Bi, M. Su, N. Li, Y. Liang, S. Dang, J. Xu, M. Hu, J. Wang, M. Zou, Y. Deng, Q. Li, S. Huang, J. Li, J. Chai, K. He, Y. H. Chen, J.-M. Zhou, The ZAR1 resistosome is a calcium-permeable channel triggering plant immune signaling. *Cell* S0092-8674(21)00600-0 (2021). doi:10.1016/j.cell.2021.05.003 Medline

22. C. Seuring, J. Greenwald, C. Wasmer, R. Wepf, S. J. Saupe, B. H. Meier, R. Riek, The mechanism of toxicity in HET-S/HET-s prion incompatibility. *PLOS Biol.* **10**, e1001451 (2012). doi:10.1371/journal.pbio.1001451 Medline

23. D. R. Herr, T. Y. A. Yam, W. S. D. Tan, S. S. Koh, W. S. F. Wong, W.-Y. Ong, K. Chayaburakul, Ultrastructural characteristics of DHA-induced pyroptosis. *Neuromolecular Med.* **22**, 293–303 (2020). doi:10.1007/s12017-019-08586-y Medline

24. J. Ding, K. Wang, W. Liu, Y. She, Q. Sun, J. Shi, H. Sun, D.-C. Wang, F. Shao, Pore-forming activity and structural autoinhibition of the gasdermin family. *Nature* **535**, 111–116 (2016). doi:10.1038/nature18590 Medline

25. M. Huysmans, S. Lema A, N. S. Coll, M. K. Nowack, Dying two deaths - programmed cell death regulation in development and disease. *Curr. Opin. Plant Biol.* **35**, 37–44 (2017). doi:10.1016/j.pbi.2016.11.005 Medline

26. W. Moeder, V. Phan, K. Yoshioka, Ca^{2+} to the rescue - Ca^{2+}channels and signaling in plant immunity. *Plant Sci.* **279**, 19–26 (2019). doi:10.1016/j.plantsci.2018.04.012 Medline

27. M. Grant, I. Brown, S. Adams, M. Knight, A. Ainslie, J. Mansfield, The RPM1 plant disease resistance gene facilitates a rapid and sustained increase in cytosolic calcium that is necessary for the oxidative burst and hypersensitive cell death. *Plant J.* **23**, 441–450 (2000). doi:10.1046/j.1365-313x.2000.00804.x Medline

28. M. J. Caterina, M. A. Schumacher, M. Tominaga, T. A. Rosen, J. D. Levine, D. Julius, The capsaicin receptor: A heat-activated ion channel in the pain pathway. *Nature* **389**, 816–824 (1997). doi:10.1038/39807 Medline

29. F. Yuan, H. Yang, Y. Xue, D. Kong, R. Ye, C. Li, J. Zhang, L. Theprungsirikul, T. Shrift, B. Krichilsky, D. M. Johnson, G. B. Swift, Y. He, J. N. Siedow, Z.-M. Pei, OSCA1 mediates osmotic-stress-evoked Ca2+ increases vital for osmosensing in *Arabidopsis*. *Nature* **514**, 367–371 (2014). doi:10.1038/nature13593 Medline

30. X. Gao, X. Chen, W. Lin, S. Chen, D. Lu, Y. Niu, L. Li, C. Cheng, M. McCormack, J. Sheen, L. Shan, P. He, Bifurcation of *Arabidopsis* NLR immune signaling via Ca(2)(+)-dependent protein kinases. *PLOS Pathog.* **9**, e1003127 (2013). doi:10.1371/journal.ppat.1003127 Medline

31. J. Castro, E. C. Aromataris, G. Y. Rychkov, G. J. Barritt, A small component of the endoplasmic reticulum is required for store-operated Ca2+ channel activation in liver cells: Evidence from studies using TRPV1 and taurodeoxycholic acid. *Biochem. J.* **418**, 553–566 (2009). doi:10.1042/BJ20081052 Medline

32. K. De Vriese, A. Costa, T. Beeckman, S. Vanneste, Pharmacological strategies for manipulating plant Ca^{2+} signalling. *Int. J. Mol. Sci.* **19**, 1506 (2018). doi:10.3390/ijms19051506 Medline

33. J. R. Inglefield, R. D. Schwartz-Bloom, Using confocal microscopy and the fluorescent indicator, 6-methoxy-N-ethylquinolinium iodide, to measure changes in intracellular chloride. *Methods Enzymol.* **307**, 469–481 (1999). doi:10.1016/S0076-6879(99)07028-7 Medline

34. H. Adachi, M. P. Contreras, A. Harant, C. H. Wu, L. Derevnina, T. Sakai, C. Duggan, E. Moratto, T. O. Bozkurt, A. Maqbool, J. Win, S. Kamoun, An N-terminal motif in NLR immune receptors is functionally conserved across distantly related plant species. *eLife* **8**, e49956 (2019). doi:10.7554/eLife.49956 Medline

35. L. Tang, T. M. Gamal El-Din, J. Payandeh, G. Q. Martinez, T. M. Heard, T. Scheuer, N. Zheng, W. A. Catterall, Structural basis for Ca2+ selectivity of a voltage-gated calcium channel. *Nature* **505**, 56–61 (2014). doi:10.1038/nature12775 Medline

36. M. Fan, J. Zhang, C.-W. Tsai, B. J. Orlando, M. Rodriguez, Y. Xu, M. Liao, M.-F. Tsai, L. Feng, Structure and mechanism of the mitochondrial Ca^{2+} uniporter holocomplex. *Nature* **582**, 129–133 (2020). doi:10.1038/s41586-020-2309-6 Medline

37. O. X. Dong, M. Tong, V. Bonardi, F. El Kasmi, V. Woloshen, L. K. Wünsch, J. L. Dangl, X. Li, TNL-mediated immunity in *Arabidopsis* requires complex regulation of the redundant ADR1 gene family. *New Phytol.* **210**, 960–973 (2016). [doi:10.1111/nph.13821](doi:10.1111/nph.13821) Medline

38. T. A. DeFalco, M. Toyota, V. Phan, P. Karia, W. Moeder, S. Gilroy, K. Yoshioka, Using GCaMP3 to study Ca2+ signaling in *Nicotiana* species. *Plant Cell Physiol.* **58**, 1173–1184 (2017). [doi:10.1093/pcp/pcx053](doi:10.1093/pcp/pcx053) Medline

39. S. Stael, P. Kmiecik, P. Willems, K. Van Der Kelen, N. S. Coll, M. Teige, F. Van Breusegem, Plant innate immunity—Sunny side up? *Trends Plant Sci.* **20**, 3–11 (2015). doi:10.1016/j.tplants.2014.10.002 Medline

40. K. Yoshioka, W. Moeder, H.-G. Kang, P. Kachroo, K. Masmoudi, G. Berkowitz, D. F. Klessig, The chimeric *Arabidopsis* CYCLIC NUCLEOTIDE-GATED ION CHANNEL11/12 activates multiple pathogen resistance responses. *Plant Cell* **18**, 747–763 (2006). [doi:10.1105/tpc.105.038786](doi:10.1105/tpc.105.038786) Medline

41. C. Zhao, Y. Tang, J. Wang, Y. Zeng, H. Sun, Z. Zheng, R. Su, K. Schneeberger, J. E. Parker, H. Cui, A mis-regulated cyclic nucleotide-gated channel mediates cytosolic calcium elevation and activates immunity in *Arabidopsis*. *New Phytol.* **230**, 1078–1094 (2021). [doi:10.1111/nph.17218](doi:10.1111/nph.17218) Medline

42. W. Tian, C. Hou, Z. Ren, C. Wang, F. Zhao, D. Dahlbeck, S. Hu, L. Zhang, Q. Niu, L. Li, B. J. Staskawicz, S. Luan, A calmodulin-gated calcium channel links pathogen patterns to plant immunity. *Nature* **572**, 131–135 (2019). [doi:10.1038/s41586-019-1413-y](doi:10.1038/s41586-019-1413-y) Medline

43. W. Gassmann, Natural variation in the *Arabidopsis* response to the avirulence gene hopPsyA uncouples the hypersensitive response from disease resistance. *Mol. Plant Microbe Interact.* **18**, 1054–1060 (2005). doi:10.1094/MPMI-18-1054 Medline

44. L. K. Mahdi, M. Huang, X. Zhang, R. T. Nakano, L. B. Kopp, I. M. L. Saur, F. Jacob, V. Kovacova, D. Lapin, J. E. Parker, J. M. Murphy, K. Hofmann, P. Schulze-Lefert, J. Chai, T. Maekawa, Discovery of a family of mixed lineage kinase domain-like proteins in plants and their role in innate immune signaling. *Cell Host Microbe* **28**, 813–824.e6 (2020). doi:10.1016/j.chom.2020.08.012 Medline

45. U. Ros, A. Peña-Blanco, K. Hänggi, U. Kunzendorf, S. Krautwald, W. W.-L. Wong, A. J. García-Sáez, Necroptosis execution is mediated by plasma membrane nanopores independent of calcium. *Cell Rep.* **19**, 175–187 (2017). doi:10.1016/j.celrep.2017.03.024 Medline

46. L. Stols, M. Gu, L. Dieckman, R. Raffen, F. R. Collart, M. I. Donnelly, A new vector for high-throughput, ligation-independent cloning encoding a tobacco etch virus protease cleavage site. *Protein Expr. Purif.* **25**, 8–15 (2002). doi:10.1006/prep.2001.1603 Medline

47. Z. Otwinowski, W. Minor, Processing of X-ray diffraction data collected in oscillation mode. *Methods Enzymol.* **276**, 307–326 (1997). [doi:10.1016/S0076-6879(97)76066-X](doi:10.1016/S0076-6879(97)76066-X)

48. P. D. Adams, D. Baker, A. T. Brunger, R. Das, F. DiMaio, R. J. Read, D. C. Richardson, J. S. Richardson, T. C. Terwilliger, Advances, interactions, and future developments in the CNS, Phenix, and Rosetta structural biology software systems. *Annu. Rev. Biophys.* **42**, 265–287 (2013). doi:10.1146/annurev-biophys-083012-130253 Medline

49. A. J. McCoy, Solving structures of protein complexes by molecular replacement with Phaser. *Acta Crystallogr. D Biol. Crystallogr.* **63**, 32–41 (2007). doi:10.1107/S0907444906045975 Medline

50. P. Emsley, B. Lohkamp, W. G. Scott, K. Cowtan, Features and development of Coot. *Acta Crystallogr. D Biol. Crystallogr.* **66**, 486–501 (2010). doi:10.1107/S0907444910007493 Medline

51. M. D. Winn, C. C. Ballard, K. D. Cowtan, E. J. Dodson, P. Emsley, P. R. Evans, R. M. Keegan, E. B. Krissinel, A. G. W. Leslie, A. McCoy, S. J. McNicholas, G. N. Murshudov, N. S. Pannu, E. A. Potterton, H. R. Powell, R. J. Read, A. Vagin, K. S. Wilson, Overview of the CCP4 suite and current developments. *Acta Crystallogr. D Biol. Crystallogr.* **67**, 235–242 (2011). doi:10.1107/S0907444910045749 Medline

52. L. Holm, L. M. Laakso, Dali server update. *Nucleic Acids Res.* **44**, W351–W355 (2016). doi:10.1093/nar/gkw357 Medline

53. M. D. Curtis, U. Grossniklaus, A gateway cloning vector set for high-throughput functional analysis of genes in planta. *Plant Physiol.* **133**, 462–469 (2003). doi:10.1104/pp.103.027979 Medline

54. S. Nakamura, S. Mano, Y. Tanaka, M. Ohnishi, C. Nakamori, M. Araki, T. Niwa, M. Nishimura, H. Kaminaka, T. Nakagawa, Y. Sato, S. Ishiguro, Gateway binary vectors with the bialaphos resistance gene, bar, as a selection marker for plant transformation. *Biosci. Biotechnol. Biochem.* **74**, 1315–1319 (2010). doi:10.1271/bbb.100184 Medline

55. C. Engler, M. Youles, R. Gruetzner, T.-M. Ehnert, S. Werner, J. D. G. Jones, N. J. Patron, S. Marillonnet, A golden gate modular cloning toolbox for plants. *ACS Synth. Biol.* **3**, 839–843 (2014). doi:10.1021/sb4001504 Medline

56. J. Schindelin, I. Arganda-Carreras, E. Frise, V. Kaynig, M. Longair, T. Pietzsch, S. Preibisch, C. Rueden, S. Saalfeld, B. Schmid, J.-Y. Tinevez, D. J. White, V. Hartenstein, K. Eliceiri, P. Tomancak, A. Cardona, Fiji: An open-source platform for biological-image analysis. *Nat. Methods* **9**, 676–682 (2012). doi:10.1038/nmeth.2019 Medline

57. K. H. Liu, Y. Niu, M. Konishi, Y. Wu, H. Du, H. Sun Chung, L. Li, M. Boudsocq, M. McCormack, S. Maekawa, T. Ishida, C. Zhang, K. Shokat, S. Yanagisawa, J. Sheen, Discovery of nitrate-CPK-NLP signalling in central nutrient-growth networks. *Nature* **545**, 311–316 (2017). doi:10.1038/nature22077 Medline

58. J. Shi, Y. Zhao, K. Wang, X. Shi, Y. Wang, H. Huang, Y. Zhuang, T. Cai, F. Wang, F. Shao, Cleavage of GSDMD by inflammatory caspases determines pyroptotic cell death. *Nature* **526**, 660–665 (2015). doi:10.1038/nature15514 Medline

59. X. Chen, W. T. He, L. Hu, J. Li, Y. Fang, X. Wang, X. Xu, Z. Wang, K. Huang, J. Han, Pyroptosis is driven by non-selective gasdermin-D pore and its morphology is different from MLKL channel-mediated necroptosis. *Cell Res.* **26**, 1007–1020 (2016). doi:10.1038/cr.2016.100 Medline

60. Z. Duxbury, S. Wang, C. I. MacKenzie, J. L. Tenthorey, X. Zhang, S. U. Huh, L. Hu, L. Hill, P. M. Ngou, P. Ding, J. Chen, Y. Ma, H. Guo, B. Castel, P. N. Moschou, M. Bernoux, P. N. Dodds, R. E. Vance, J. D. G. Jones, Induced proximity of a TIR signaling domain on a

plant-mammalian NLR chimera activates defense in plants. *Proc. Natl. Acad. Sci. U.S.A.* **117**, 18832–18839 (2020). doi:10.1073/pnas.2001185117 Medline

61. T. Katsumoto, T. Naguro, A. Iino, A. Takagi, The effect of tannic acid on the preservation of tissue culture cells for scanning electron microscopy. *J. Electron Microsc. (Tokyo)* **30**, 177–182 (1981). Medline

62. Z. M. Pei, Y. Murata, G. Benning, S. Thomine, B. Klüsener, G. J. Allen, E. Grill, J. I. Schroeder, Calcium channels activated by hydrogen peroxide mediate abscisic acid signalling in guard cells. *Nature* **406**, 731–734 (2000). [doi:10.1038/35021067](doi:10.1038/35021067) Medline

63. S. M. Collier, L. P. Hamel, P. Moffett, Cell death mediated by the N-terminal domains of a unique and highly conserved class of NB-LRR protein. *Mol. Plant Microbe Interact.* **24**, 918–931 (2011). doi:10.1094/MPMI-03-11-0050 Medline

64. T. L. Bailey, C. Elkan, Fitting a mixture model by expectation maximization to discover motifs in biopolymers. *Proc. Int. Conf. Intell. Syst. Mol. Biol.* **2**, 28–36 (1994). Medline

65. T. L. Bailey, M. Gribskov, Combining evidence using p-values: Application to sequence homology searches. *Bioinformatics* **14**, 48–54 (1998). doi:10.1093/bioinformatics/14.1.48 Medline

66. W. J. Thomas, C. A. Thireault, J. A. Kimbrel, J. H. Chang, Recombineering and stable integration of the *Pseudomonas syringae* pv. *syringae* 61 *hrp/hrc* cluster into the genome of the soil bacterium *Pseudomonas fluorescens* Pf0-1. *Plant J.* **60**, 919–928 (2009). [doi:10.1111/j.1365-313X.2009.03998.x](doi:10.1111/j.1365-313X.2009.03998.x) Medline